Collective phenomena in a quasi-two-dimensional system of fermionic polar molecules: Band renormalization and excitons

Mehrtash Babadi and Eugene Demler
Physics Department, Harvard University, Cambridge, Massachusetts 02138, USA
(Received 7 July 2011; published 26 September 2011)

We theoretically analyze a quasi-two-dimensional system of fermionic polar molecules trapped in a harmonic transverse confining potential. The renormalized energy bands are calculated by solving the Hartree-Fock equation numerically for various trap and dipolar interaction strengths. The intersubband excitations of the system are studied in the conserving time-dependent Hartree-Fock (TDHF) approximation from the perspective of lattice modulation spectroscopy experiments. We find that the excitation spectrum consists of both intersubband particle-hole excitation continua and antibound excitons whose antibinding behavior is associated to the anisotropic nature of dipolar interactions. The excitonic modes are shown to capture the majority of the spectral weight. We evaluate the intersubband transition rates in order to investigate the nature of the excitonic modes and find that they are antibound states formed from particle-hole excitations arising from several subbands. We discuss the sum rules in the context of lattice modulation spectroscopy experiments and utilize them to check the consistency of the obtained results. Our results indicate that the excitonic effects persist for interaction strengths and temperatures accessible in the current experiments with polar molecules.

DOI: 10.1103/PhysRevA.84.033636 PACS number(s): 67.85.Lm, 71.20.−b, 71.35.Cc

I. INTRODUCTION

In the past decade, much of the experimental and theoretical progress in the field of ultracold atoms [1–3] has been motivated by the prospect of realizing novel strongly correlated many-body states of matter. In particular, the experimental realization of quantum degenerate gases of fermionic polar molecules has witnessed a very rapid progress. By association of atoms via a Feshbach resonance to form deeply bound ultracold molecules [4,5], a nearly degenerate gas of KRb polar molecules in their rotational and vibrational ground state has been recently realized [6–10]. The molecules can be polarized by applying a dc electric field, resulting in strong dipole-dipole intermolecular interactions.

A strikingly new feature of systems of fermionic polar molecules is the anisotropy of dipolar interactions, making them unparalleled among the traditional condensed matter systems. The experiments with ultracold polar molecules thus go beyond quantum simulation of effective theories motivated by electronic systems and aim at exploring a genuinely new domain of many-body quantum behavior, unique to dipolar interactions. Dipolar interactions can be utilized to generate long-range interactions of different shapes using microwave fields [11], simulate exotic spin Hamiltonians [12,13], and are theoretically predicted to give rise to numerous interesting collective phenomena such as roton softening [14–16], supersolidity [17–21], p-wave superfluidity [22], emergence of artificial photons [23], bilayer quantum phase transitions [24], multilayer self-assembled chains [25] for bosonic molecules, dimerization and interlayer pairing [26,27], spontaneous interlayer coherence [28], ferroelectricity [29,30], anisotropic Fermi liquid theory and anisotropic sound modes [31–34], fractional quantum Hall effect [35], Wigner crystallization [36], density-wave and striped order [37,38], biaxial nematic phase [39], topological superfluidity [40], and Z_2 topological phase [41], just to mention a few.

Despite the theoretical prediction of numerous exotic quantum many-body phenomena in polar molecules, the realization and observation of many of these novel predictions is still an experimental challenge. At the time this paper was written, the coldest gas of fermionic polar molecules has been realized with KRb molecules at a temperature of $1.4T_F$ [6–10], where T_F is the Fermi temperature. The majority of the quantum phenomena mentioned require strong suppression of thermal fluctuations; that is, a strong quantum degeneracy condition ($T \ll T_F$).

A major obstacle toward further evaporative cooling of a large class of bialkali polar molecules (KRb, LiNa, LiK, LiRb, and LiCs) is the existence of an energetically allowed two-body chemical reaction channel [42], resulting in a significant molecule loss in two-body scatterings. In a low-temperature gas composed of a single hyperfine state, Fermi statistics blocks scatterings in the s-wave channel and the majority of scatterings take place through the p-wave channel. In unstructured three-dimensional clouds, the attractive head-to-tail dipolar interactions soften the p-wave centrifugal barrier and increase the rate of chemical reactions. However, the rate of chemical reactions can be effectively suppressed by loading the gas into a one-dimensional optical lattice (or trap) and aligning the dipoles perpendicular to the formed pancakes. In such geometries, the incidence of head-to-tail scatterings is effectively suppressed due to the transverse confinement of the gas on one hand, and reinforcement of the p-wave barrier occurs due to repulsive side-by-side dipolar interactions on the other hand [9,43,44]. Therefore, the preferred geometry to study reactive polar molecules is in tightly confined two-dimensional layers.

Recently, it has been shown that the suppression of chemical reactions of reactive fermionic molecules in confined geometries remains effective even in the quasi-two-dimensional limit; that is, where not only the lowest, but also the first few excited subbands (higher transverse modes) are populated [44]. Occupation of higher subbands does not impose any difficulty on experiments with nonreactive molecules such as NaK, NaRb, NaCs, KCs, and RbCs [42]. The possibility of going

beyond the single-subband limit opens a new window toward experimental and theoretical exploration of the many-body physics of quasi-two-dimensional fermions with anisotropic interactions.

Besides being highly anisotropic, fermionic polar molecules and electronic systems differ in another important way: in contrast to the Coulomb interactions, dipole-dipole interactions dominate the kinetic energy in the high-density limit. In d dimensions, the dipolar interaction scales as $n^{3/d}$ (n is the density) while the kinetic energy scales as $n^{2/d}$, implying that their ratio scales as $n^{1/d}$ (i.e., the interactions are more pronounced at higher densities). We define the following dimensionless quantity as a measure of the dipolar interaction strength in two dimensions:

$$r_d \equiv \frac{mD^2 n^{1/2}}{\hbar^2}, \tag{1}$$

where D is the electric dipole moment of a single molecule.

The main goal of this paper is to study the intersubband collective modes of quasi-two-dimensional polar molecules and to propose experimental signatures of such phenomena. At the time this paper was written, the dipolar interaction strengths accessible in experiments belong to the weakly interacting regime (e.g., $r_d \approx 0.05$ in experiments of the group at JILA) and, therefore, we restrict our analysis to the same regime. For small r_d, the normal liquid phase is expected to be the stable phase of the system.

In the first part of this paper, we study the effect of dipolar interactions on the single-particle energy dispersions by solving the Hartree-Fock equation. In order to simplify our analysis, we focus on a single pancake and neglect complications such as interlayer tunneling and attractive interlayer interactions in this study. This approximation is relevant to molecules in a strong transverse trap, as well as well-separated stack of pancakes realized in a strong optical lattice. The normal phase and the collective modes of fermionic polar molecules in the strictly two-dimensional case (single-subband limit) has been recently studied by different authors [22,34,37]. Thus, we do not discuss the intrasubband collective modes here and only focus on collective modes unique to the multisubband limit.

In the second part of this paper, we explore the intersubband excitation spectrum from the lattice modulation spectroscopy perspective, which is an experimental technique originally developed for studying strongly correlated phases of cold atomic systems [45–49]. We predict the energy absorption and intersubband transition rates for weak modulation pulses in the conserving time-dependent Hartree-Fock (TDHF) approximation [50]. We consider finite pulse duration which allows us to go beyond the usual approximation of Fermi's golden rule. We find that the excitation spectrum consists of both intersubband particle-hole (p-h) excitation continua and antibound excitons arising from the anisotropic nature of dipolar interactions. We show that these many-body effects persist for weak interactions and temperatures of the order of the Fermi temperature, making their observation feasible in current experiments.

Studying the intersubband transition rates sheds light on the mechanism of energy absorption at various parts of the energy absorption spectrum. In particular, we find that, while the p-h continua are associated to p-h excitations between two definite subbands, the excitonic modes are formed from p-h excitations arising from more than one subband.

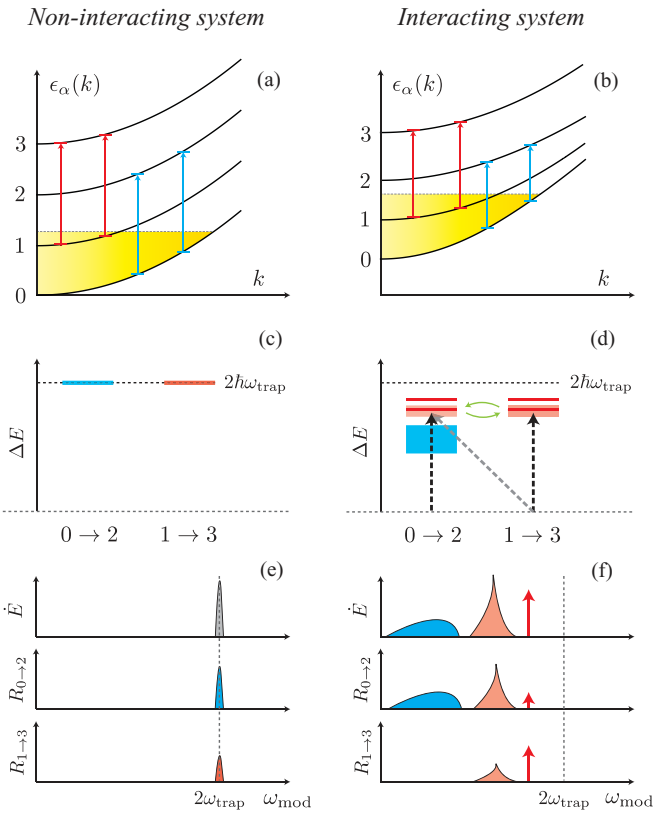

FIG. 1. (Color online) Comparison between quasi-two-dimensional fermions in the absence (left column) and presence (right column) of interactions. Panels (a) and (b) show a schematic plot of the band structure. The blue (rightmost) and red (leftmost) arrows indicate p-h excitations from 0 to 2 and subbands 1 to 3, respectively, at different parts of the Fermi sea. Panels (c) and (d) show a schematic representation of excited states probed in modulation spectroscopy experiments. The labels, $0 \to 2$ and $1 \to 3$, indicate the intersubband transition associated to the excitation. The blue (bottom) and red (top) intervals denote p-h continua and the red lines denote excitonic modes. Panels (e) and (f) show the energy absorption rate $\dot{E}$ and intersubband transition rates $R_{0\to2}$ and $R_{1\to3}$ as a function of modulation frequency $\omega_{\rm mod}$. The blue (darker) and red (lighter) shaded continua correspond to $0 \to 2$ and $1 \to 3$ intersubband transitions, respectively. The red spike denotes an exciton. The kink in the middle of the red shaded continuum indicates an exciton lying inside that continuum [see plots in panels (c) and (d)]. Refer to the text for more details.

Before we embark on the formal development of the outlined program, we find it worthwhile to summarize the results obtained in a schematic way. Figure 1 shows a side by side comparison between noninteracting and interacting quasi-two-dimensional fermions with dipolar interactions. A typical plot of the band structure is shown in Figs. 1(a) and 1(b). In the absence of interactions, the single-particle energy dispersions are quadratic and have a constant energy separation of $\hbar\omega_{\rm trap}$, where $\omega_{\rm trap}$ is the trap frequency. In the presence of interactions, the single-particle energy dispersions are renormalized and no longer remain quadratic. Band renormalization broadens the intersubband excitation spectrum.

Modulation of the optical lattice stimulates excitation of particles from populated subbands in equilibrium to their second next subband ($0 \to 2$, $1 \to 3$, etc.). The excitation energy of such processes can be directly measured in the experiments. In the absence of interactions, all of the elementary intersubband excitations have a constant energy cost of $2\hbar\omega_{\rm trap}$. The interactions modify the degenerate excited states dramatically, transforming the p-h excitation energies from their constant value of $2\hbar\omega_{\rm trap}$ to a collection of continua and discrete collective modes (excitons), as shown in Figs. 1(c) and 1(d). It turns out that the excitonic modes capture the majority of the spectral weight, leaving behind only a small trace of the p-h continua.

As mentioned earlier, the mechanism of energy absorption in lattice modulation experiments can be explored further by studying the intersubband transition rates in modulation experiments. If the modulation frequency lies within a certain intersubband p-h excitation continuum, we expect to observe transitions only between the two involved subbands, leaving the population of other subbands unaffected. For example, the blue (dark) shaded continuum in the energy absorption spectrum in Figs. 1(d) and 1(f) is associated to $0 \to 2$ excitations and, consequently, the continuum only appears in the plot of $R_{0\to 2}$ and is absent in the plot of $R_{1\to 3}$ vs modulation frequency, where $R_{\alpha\to\beta}$ denotes the net current from the α to β Hartree-Fock subband.

If the modulation frequency corresponds to an excitonic mode, we expect to observe transition currents between several pairs of subbands (we will show later that the excitons are generally mixtures of p-h excitations arising from more than a single subband). For example, the red spike in the energy absorption spectrum, which denotes an exciton, is visible in both $R_{0\to 2}$ and $R_{1\to 3}$ plots.

Finally, if an exciton lies inside a continuum, it will be damped and yield a broadened peak in the energy absorption spectrum. In this case, although the continuum is associated to a certain intersubband transition *per se*, mixing with the excitonic mode results in its participation in several other intersubband transitions as well. This effect is schematically shown in Figs. 1(d) and 1(f). The red (light) shaded continuum in the energy absorption spectrum denotes a $1 \to 3$ p-h continuum and the kink in the middle is indicative of an exciton lying inside it. Both the continuum and the kink appear in all of the intersubband transition-rate plots in this case.

We explore the ideas summarized above in detail in the remainder of this paper. This paper is organized as follows: The microscopic model is introduced in Sec. II and the Hartree-Fock equation is discussed in Sec. III. The numerical results obtained by solving the Hartree-Fock equation is discussed in Sec. III A. The lattice modulation spectroscopy is reviewed in Sec. IV and the calculation of the energy absorption spectrum and intersubband transition rates in the TDHF approximation is discussed in Sec. IV A. The numerical results are presented and discussed in Sec. IV C. The paper is concluded by a short discussion on the experimental outlook of the presented results.

II. THE MICROSCOPIC MODEL

In this section, we review the microscopic model for one-component fermionic polar molecules in a harmonic transverse confining potential. The model is relevant to a single pancake of polar molecules as well as a well-separated stack of pancakes.

For concreteness, we assume that the gas is confined about the x-y plane using a confining optical potential centered at $z = 0$. Also, we assume that the dipoles are aligned along the z axis (perpendicular to the confining plane) using a strong dc electric field. The Hamiltonian of the system is the sum of the optical trap potential, the kinetic energy and the electric dipole-dipole interactions. A convenient basis for the second-quantized notation is one that diagonalizes the one-body part of the Hamiltonian. We choose the following basis:

$$\langle \mathbf{r}|\alpha,\mathbf{k}\rangle = \phi_\alpha(z)\frac{1}{\sqrt{A}}e^{i\mathbf{k}\cdot\mathbf{x}}, \tag{2}$$

where $\phi_\alpha(z)$ is the wave function of transverse mode α of the trap, A is the area of the trap in the x-y plane, and $\mathbf{x} = (x,y)$ is the in-plane coordinates. In this basis, the second-quantized Hamiltonian is easily found to be

$$H = \sum_{\mathbf{k},\alpha}\left(\frac{\hbar^2|\mathbf{k}|^2}{2m} + \epsilon_\alpha\right)c^\dagger_{\mathbf{k},\alpha}c_{\mathbf{k},\alpha} + \frac{1}{2}\sum_{\alpha\beta;\gamma\lambda}\sum_{\mathbf{k}_1\mathbf{k}_2\mathbf{q}}\mathcal{V}_{\alpha\beta;\gamma\lambda}(\mathbf{q})c^\dagger_{\mathbf{k}_1+\mathbf{q},\alpha}c^\dagger_{\mathbf{k}_2-\mathbf{q},\gamma}c_{\mathbf{k}_2,\lambda}c_{\mathbf{k}_1,\beta}, \tag{3}$$

where $c_{\mathbf{k},\alpha}$ ($c^\dagger_{\mathbf{k},\alpha}$) annihilates (creates) a particle in the in-plane momentum state $\mathbf{k}$ and in subband α. ϵ_α is the zero-point energy of subband α ($\alpha = 0,1,\ldots$). We measure the energies with respect to the zero-point energy of the lowest subband ($\alpha = 0$). $\mathcal{V}_{\alpha\beta;\gamma\lambda}(\mathbf{q})$ is the Fourier transform of the effective intersubband dipolar interaction, defined as

$$V_{\alpha\beta;\gamma\lambda}(\mathbf{x}-\mathbf{x}') = \int\int dz dz' \phi^*_\alpha(z)\phi^*_\gamma(z')\phi_\lambda(z')\phi_\beta(z) \times V_{\rm dip}(z-z',\mathbf{x}-\mathbf{x}'), \tag{4}$$

where $V_{\rm dip}(z,\mathbf{x})$ is the electric dipole-dipole interaction of two particles with a center separation of $(z,\mathbf{x})$:

$$V_{\rm dip}(z,\mathbf{x}) = \frac{D^2}{(|\mathbf{x}|^2+z^2)^{\frac{5}{2}}}(|\mathbf{x}|^2 - 2z^2). \tag{5}$$

The intrasubband interactions are special cases of Eq. (4); that is, the intrasubband interaction in subband α is given by $\mathcal{V}_{\alpha\alpha;\alpha\alpha}(\mathbf{q})$. Since the dipoles are perpendicular to the x-y plane, the interaction matrix elements are isotropic in the in-plane momentum $\mathbf{q}$.

One can always choose the transverse wave functions $\phi_\alpha(z)$ to be real and of well-defined parity for trap potentials which are symmetric about $z = 0$ (a harmonic trap is one example). As a result, it is easy to verify that $\mathcal{V}_{\alpha\beta;\gamma\lambda}$ is invariant under the following interchange of indices: $\alpha \leftrightarrow \beta$, $\gamma \leftrightarrow \lambda$, or $\alpha\beta \leftrightarrow \gamma\lambda$. Also, $\mathcal{V}_{\alpha\beta;\gamma\lambda}$ vanishes if $\alpha+\beta+\gamma+\lambda \equiv 1 \pmod 2$. This parity-conserving behavior is due to the invariance of Eq. (5) under the inversion $z \to -z$ and breaks down if the dipoles are not aligned perpendicular to the trap plane.

For simplicity, we assume that the optical trap is perfectly harmonic with a frequency $\omega_{\rm trap}$. In this case, we easily find

$$\epsilon_\alpha = \alpha(\hbar\omega_{\rm trap}), \qquad \phi_\alpha(z) = \frac{1}{\sqrt{\pi^{1/2}\alpha!2^\alpha a_\perp}}H_\alpha(z/a_\perp)e^{-z^2/(2a_\perp)}, \tag{6}$$

where $H_\alpha(z)$ is the Hermite polynomial of degree α [51] and $a_\perp$ is the transverse confinement width and is related to the trap frequency as $\omega_{\rm trap} = \hbar/(ma_\perp^2)$. A generating function for $\mathcal{V}_{\alpha\beta;\gamma\lambda}(\mathbf{q})$ for harmonic traps is derived in Appendix A and explicit expressions for the first few intersubband interactions are given.

We note that, in the experiments, nearly perfect harmonic trapping can be achieved by loading the gas into a single well of a strong optical lattice. An optical lattice potential of the form $V_{\rm lat}(z) = [\hbar^2/(2ma_\perp^4 k^2)]\sin^2 kz$ yields a harmonic trap with frequency $\hbar/(ma_\perp^2)$ centered at $z = 0$ in the limit $k \to 0$.

III. HARTREE-FOCK EQUATION FOR UNIFORM QUASI-TWO-DIMENSIONAL FERMIONIC GAS

We briefly review the Hartree-Fock (HF) theory for a uniform quasi-two-dimensional fermionic gas in thermal equilibrium and apply the formalism to the system of fermionic polar molecules. The Hartree-Fock equation for quasi-two-dimensional systems is found to be more difficult to solve compared to the strictly two-dimensional case due to subband hybridization. A similar situation arises in the HF study of two-component Fermi gases with effective magnetic dipole-dipole interactions [52].

We begin our treatment with the usual definition of the one-particle thermal Green's function:

$$\mathcal{G}_{\mu\nu}(\mathbf{k}, i\omega_n) = -\int_0^{\beta\hbar} d\tau e^{i\omega_n\tau}\mathrm{Tr}[\hat{\rho}_{\rm G} c_{\mathbf{k},\mu}(\tau) c^\dagger_{\mathbf{k},\nu}(0)], \qquad (7)$$

where $\beta = 1/(k_B T)$, T is the temperature, $i\omega_n = (2n+1)\pi/\beta$ is the fermionic Matsubara frequency, $\hat{\rho}_{\rm G} = e^{-\beta H}/\mathrm{Tr}[e^{-\beta H}]$ is the grand-canonical thermal equilibrium weighting operator, and $c^{(\dagger)}_{\mathbf{k},\mu}(\tau) = e^{\tau H/\hbar} c^{(\dagger)}_{\mathbf{k},\mu} e^{-\tau H/\hbar}$ is the imaginary-time Heisenberg fermion annihilation (creation) operator. In the presence of interactions, the noninteracting subband indices no longer remain good quantum numbers due to hybridization and, consequently, $\mathcal{G}_{\mu\nu}(\mathbf{k}, i\omega_n)$ is expected to have nonzero off-diagonal elements.

The Hartree-Fock approximation for the Green's function is given by the following diagrammatic Dyson's equation [53]:

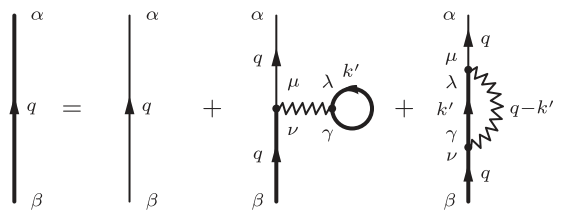

(8)

where the thin and thick fermion lines denote noninteracting and interacting Green's functions, respectively. The diagram yields the following equation:

$$\mathcal{G}_{\alpha\beta}(\mathbf{k}, i\omega_n) = \mathcal{G}^0_{\alpha\beta}(\mathbf{k}, i\omega_n) + \mathcal{G}^0_{\alpha\mu}(\mathbf{k}, i\omega_n)\Sigma^\star_{\mu\nu}(\mathbf{k})\mathcal{G}_{\nu\beta}(\mathbf{k}, i\omega_n), \qquad (9)$$

where the proper self-energy $\Sigma^\star_{\mu\nu}(\mathbf{k})$ is the sum of the direct and exchange diagrams:

$$\Sigma^\star_{\mu\nu}(\mathbf{k}) = \frac{1}{\beta}\sum_{i\omega'_n}\int \frac{d^2\mathbf{k}'}{(2\pi)^2}[\mathcal{V}_{\mu\nu;\gamma\lambda}(0) - \mathcal{V}_{\mu\lambda;\gamma\nu}(\mathbf{k}-\mathbf{k}')] \times \mathcal{G}_{\lambda\gamma}(\mathbf{k}', i\omega'_n)e^{i\omega'_n 0^+}. \qquad (10)$$

Summation over repeated indices is assumed throughout this paper. The noninteracting thermal Green's function is given by

$$\mathcal{G}^0_{\alpha\beta}(\mathbf{k}, i\omega_n) = \frac{\delta_{\alpha\beta}}{i\omega_n - \xi_{\mathbf{k},\alpha}}, \quad \xi_{\mathbf{k},\alpha} = \frac{|\mathbf{k}|^2}{2m} + \epsilon_\alpha - \mu. \qquad (11)$$

In the absence of spontaneous symmetry breaking of the inversion symmetry (which may happen in the strongly interacting regime and is beyond the scope of this paper), the interactions only mix subbands of the same parity due to the symmetries of the intersubband interaction matrix elements mentioned in the previous section. Investigating Eqs. (9) and (10) shows that $\mathcal{G}_{\alpha\beta} = 0$ if $\alpha + \beta \equiv 1 \pmod 2$ and therefore, $\mathcal{G}_{\alpha\beta}$ will have the following matrix structure in the noninteracting subband indices:

$$\mathcal{G} = \begin{pmatrix} \mathcal{G}_{00} & 0 & \mathcal{G}_{02} & 0 & \mathcal{G}_{04} & \cdots \\ 0 & \mathcal{G}_{11} & 0 & \mathcal{G}_{13} & 0 & \cdots \\ \mathcal{G}_{02} & 0 & \mathcal{G}_{22} & 0 & \mathcal{G}_{24} & \cdots \\ 0 & \mathcal{G}_{13} & 0 & \mathcal{G}_{33} & 0 & \cdots \\ \mathcal{G}_{04} & 0 & \mathcal{G}_{24} & 0 & \mathcal{G}_{44} & \cdots \\ \vdots & \vdots & \vdots & \vdots & \vdots & \ddots \end{pmatrix}. \qquad (12)$$

In order to solve the Hartree-Fock equation at finite temperatures, one must carry out the Matsubara frequency summations appearing in Eq. (10). The summation can be easily done once the dependence of the Green's function on the Matsubara frequency is explicitly known. This can be done by expressing the interacting Green's function in its diagonal basis. Treated as a matrix equation, Eq. (9) formally yields

$$\mathcal{G} = [(\mathcal{G}^0)^{-1} - \Sigma^\star]^{-1} = [i\omega_n \mathbf{I} - \overline{\Sigma}^\star]^{-1}, \qquad (13)$$

where $\overline{\Sigma}^\star_{\alpha\beta}(\mathbf{k}) = \Sigma^\star_{\alpha\beta}(\mathbf{k}) + \xi^0_{\mathbf{k},\alpha}\delta_{\alpha\beta}$ (i.e., the proper self-energy including the kinetic energy contribution). It is easy to see that $\overline{\Sigma}^\star(\mathbf{k})$ is a symmetric matrix and, therefore, it has real eigenvalues and there exists a real, complete, and orthonormal basis in which it is diagonal. Let $U(\mathbf{k})$ be the orthogonal transformation that diagonalizes $\overline{\Sigma}^\star(\mathbf{k})$:

$$\overline{\Sigma}^\star(\mathbf{k}) = U(\mathbf{k})\Xi(\mathbf{k})U^T(\mathbf{k}), \quad \Xi(\mathbf{k}) = \mathrm{diag}\{\tilde{\xi}_1(\mathbf{k}), \tilde{\xi}_2(\mathbf{k}), \ldots\}, \qquad (14)$$

where $\{\tilde{\xi}_\alpha(\mathbf{k})\}$ are the eigenvalues. The same transformation clearly diagonalizes the interacting Green's function:

$$\tilde{\mathcal{G}}_{\alpha\beta}(\mathbf{k}, i\omega_n) \overset{\rm def}{=} [U(\mathbf{k})^T \mathcal{G} U(\mathbf{k})]_{\alpha\beta} = [i\omega_n \mathbf{I} - \Xi(\mathbf{k})]^{-1}_{\alpha\beta} = \frac{\delta_{\alpha\beta}}{i\omega_n - \tilde{\xi}_\alpha(\mathbf{k})}. \qquad (15)$$

As promised, the Matsubara frequency summation appearing in Eq. (10) can be evaluated with ease in the new basis:

$$\begin{aligned}\frac{1}{\beta}\sum_{i\omega_n'}\mathcal{G}_{\lambda\gamma}(\mathbf{k}',i\omega_n')e^{i\omega_n'0^+} &= \frac{1}{\beta}\sum_{i\omega_n'}\sum_{\rho}U_{\lambda\rho}(\mathbf{k}')U_{\gamma\rho}(\mathbf{k}')\frac{e^{i\omega_n'0^+}}{i\omega_n'-\tilde{\xi}_\rho(\mathbf{k}')}\\ &= \sum_{\rho}U_{\lambda\rho}(\mathbf{k}')n^F[\tilde{\xi}_\rho(\mathbf{k}')]U_{\gamma\rho}(\mathbf{k}'),\end{aligned}\tag{16}$$

where $n^F(x)=(e^{\beta x}+1)^{-1}$ is the Fermi occupation function, resulting from the summation over fermionic Matsubara frequencies [53]. Plugging this result into Eq. (9), we reach an explicit self-consistent equation for the proper self-energy:

$$\begin{aligned}\Sigma^\star_{\mu\nu}(\mathbf{k}) = \int\frac{d^2\mathbf{k}'}{(2\pi)^2}[\mathcal{V}_{\mu\nu;\gamma\lambda}(0)-\mathcal{V}_{\mu\lambda;\gamma\nu}(\mathbf{k}-\mathbf{k}')]U_{\lambda\rho}(\mathbf{k}')\\ \times U_{\gamma\rho}(\mathbf{k}')n^F[\xi_\rho(\mathbf{k}')].\end{aligned}\tag{17}$$

It is understood that $U(\mathbf{k})$ and $\xi_\rho(\mathbf{k})$ are implicit functions of $\Sigma^\star(\mathbf{k})$, defined in Eq. (14).

It is clear from the preceding discussion that the orthogonal transformation $U(\mathbf{k})$ also defines the mean-field single-particle states in the presence of interactions. We identify $\tilde{\xi}_\alpha(\mathbf{k})$ as the energy dispersion of Hartree-Fock subband α and define the Hartree-Fock fermion annihilation (creation) operators as

$$\tilde{c}^{(\dagger)}_{\mathbf{k},\alpha}(\tau)=\sum_{\mu}U_{\mu\alpha}(\mathbf{k})c^{(\dagger)}_{\mathbf{k},\mu}(\tau).\tag{18}$$

It is straightforward to show, in light of Eq. (15), that $\tilde{\mathcal{G}}_{\mu\nu}(\mathbf{k},i\omega_n)$ can be identically defined using the Hartree-Fock fermion operators:

$$\tilde{\mathcal{G}}_{\mu\nu}(\mathbf{k},i\omega_n)=-\int_0^{\beta\hbar}d\tau e^{i\omega_n\tau}\mathrm{Tr}\big[\hat{\rho}_{\mathrm{G}}^{\mathrm{HF}}\tilde{c}_{\mathbf{k},\mu}(\tau)\tilde{c}^\dagger_{\mathbf{k},\nu}(0)\big],\tag{19}$$

where $\hat{\rho}_{\mathrm{G}}^{\mathrm{HF}}$ is the grand-canonical operator defined in terms of the Hartree-Fock decoupled Hamiltonian.

At this point, it is also useful to define the effective interaction between Hartree-Fock quasiparticles. It is more natural to evaluate the response functions in this basis, which is our goal in the second part of this study. Expressing the interaction part of the Hamiltonian in terms of Hartree-Fock fermion operators, one can easily read off the renormalized interaction between incoming particles in Hartree-Fock subbands β and λ with momenta $\mathbf{k}_1$ and $\mathbf{k}_2$, scattering to subbands α and γ with momenta $\mathbf{k}_1+\mathbf{q}$ and $\mathbf{k}_2-\mathbf{q}$, respectively:

$$\begin{aligned}\tilde{\mathcal{V}}_{\alpha\beta;\gamma\lambda}(\mathbf{k}_1,\mathbf{k}_2,\mathbf{q}) = \sum_{\alpha'\beta'\gamma'\lambda'}\mathcal{V}_{\alpha'\beta';\gamma'\lambda'}(\mathbf{q})U_{\alpha'\alpha}(\mathbf{k}_1+\mathbf{q})\\ \times U_{\gamma'\gamma}(\mathbf{k}_2-\mathbf{q})U_{\lambda'\lambda}(\mathbf{k}_2)U_{\beta'\beta}(\mathbf{k}_1).\end{aligned}\tag{20}$$

Note that the interaction between Hartree-Fock quasiparticles is no longer just a function of the momentum transfer, but also depends on the individual momenta of the scattering quasiparticles.

A. Results: renormalized bands

In this section, we present the numerical results obtained by solving the Hartree-Fock equation. The numerical method is described in Appendix B in detail. The temperatures are reported in units of T^*, which is defined as

$$T^*=\hbar^2n/(2mk_B).\tag{21}$$

T^* is related to $T_F^{(0)}$, the Fermi temperature of a two-dimensional noninteracting Fermi gas, as

$$T^*=T_F^{(0)}/(4\pi)\simeq 0.08T_F^{(0)}.\tag{22}$$

Figure 2 shows the energies of the first five Hartree-Fock subbands [panels (a), (c), and (e)] and their corresponding density of states (DOS) [panels (b), (d), and (f)] for $r_d=1.0$, $T/T^*=0.1$, and for three different transverse confinement widths $\sqrt{n}a_\perp=0.2$, 0.4, and 0.6. Deviations from the noninteracting quadratic energy dispersions can also be observed in the DOS plots: the DOS of a quasi-two-dimensional noninteracting Fermi gas has a uniform staircase structure [shown in Figs. 2(b), 2(d), and 2(f) with dashed lines for reference]. In the presence of interactions, we find that (1) the DOS plot starts at a finite energy, meaning that the zero-point energy of the lowest subband is lifted, (2) the DOS plot no longer has flat regions (due to deviations from quadratic), (3) the energy spacing between the jumps, which correspond

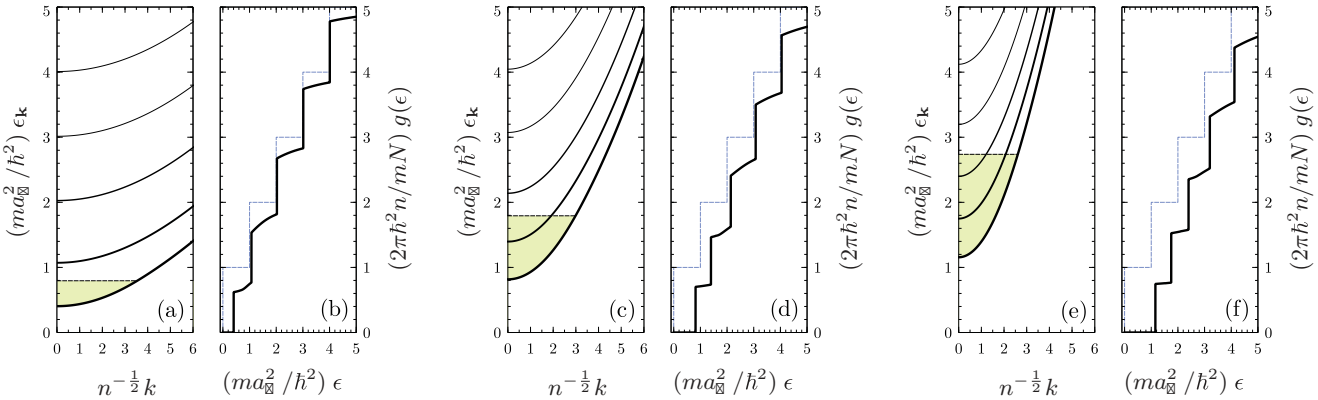

FIG. 2. (Color online) Energy dispersion of the first five Hartree-Fock subbands [panels (a), (c), and (e)] and the density of states (DOS) $g(\epsilon)$ [panels (b), (d), and (f)] for $r_d=1.0$ and $T/T^*=0.1$. Panels (a) and (b): $\sqrt{n}a_\perp=0.2$. Panels (c) and (d): $\sqrt{n}a_\perp=0.4$. Panels (e) and (f): $\sqrt{n}a_\perp=0.6$. The DOS in the absence of interactions is also shown for comparison (blue dashed lines).

to the spacing between the zero-point energies of the subbands, become nonuniform, and (4) the DOS of the interacting gas is always lower than the DOS of the noninteracting gas, which is associated to the long-range repulsive nature of dipolar interactions in the confined geometry studied.

At zero temperature, the occupation of higher subbands is only due to Pauli exclusion and the Fermi occupation function is sharp. Therefore, at any given density, trap strength, and interaction strength, only a finite number of Hartree-Fock subbands are fully or partially occupied. A phase diagram can thus be obtained for the system at $T = 0$ as a function of trap and dipolar interaction strengths (Fig. 4). The diagram shows that, at fixed transverse confinement width $a_\perp$ and density n, increasing the interaction results in occupation of higher subbands. This behavior can be understood in light of the reduction of the DOS due to interactions. The energy and fractional occupation of the subbands were found to be continuous across the phase boundaries and, therefore, the transitions are continuous. The same transitions have been reported to be first-order for a quasi-two-dimensional electron gas [54].

In order to see the hybridization of noninteracting subbands, we have plotted the fractional density of noninteracting and Hartree-Fock subbands in Figs. 3(a) and 3(b), respectively, as a function of transverse confinement width and at fixed $r_d = 0.05$ and temperature $T/T^* = 0.1$. Figures 3(c) and 3(c) show the same quantities at a higher temperature $T/T^* = 1.0$. It is observed that larger transverse confinement widths (i.e., weaker traps) naturally result in the occupation of higher subbands. Hybridization is clearly noticeable by comparing Fig. 3(a) with Fig. 3(b): occupation of the lowest Hartree-Fock subband amounts to occupation of several noninteracting subbands of even parity, $0, 2, 4, \ldots$, with decreasing weights. A consequence of subband mixing is anomalous population inversion; that is, the second noninteracting subband is populated

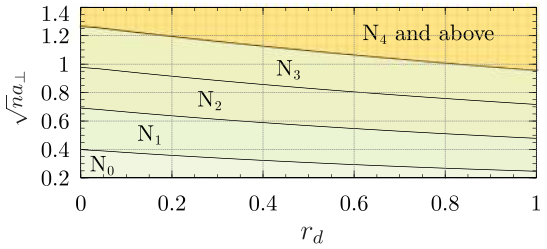

FIG. 4. (Color online) Quasi-two-dimensional liquid phases of fermionic polar molecules at $T = 0$. The abbreviations N_0, N_1, etc. stand for normal liquid phases populating up to the zeroth, first, . . .Hartree-Fock subbands respectively.

before the first noninteracting subband due to hybridization with subbands 0, 4, . . .

Finally, Fig. 3(e) shows the renormalized chemical potential as a function of transverse confinement width at three different temperatures (solid lines). We have also plotted the chemical potential in the absence of interactions for reference (dashed lines). We find that the renormalized chemical potential is always greater than its noninteracting value, which is again due to reduction of the DOS in the presence of interactions. An interesting observation is the nonmonotonic behavior of the chemical potential as a function of temperature, which is clearly noticeable in the inset plot of Fig. 3(e). As a consequence, the isothermal compressibility of the interacting gas, $\kappa_T = n^{-2}(\partial n/\partial\mu)_T$, will be a nonmonotonic function of temperature. This behavior has been reported earlier [55] and is also confirmed by our calculations. Intuitively, a small rise in temperature will result in thermal excitation of states just below the Fermi level. Having larger momenta, the thermally excited quasiparticles experience stronger interactions and decrease the DOS at the Fermi level. At a fixed number of particles, the chemical potential has to be increased in order to compensate

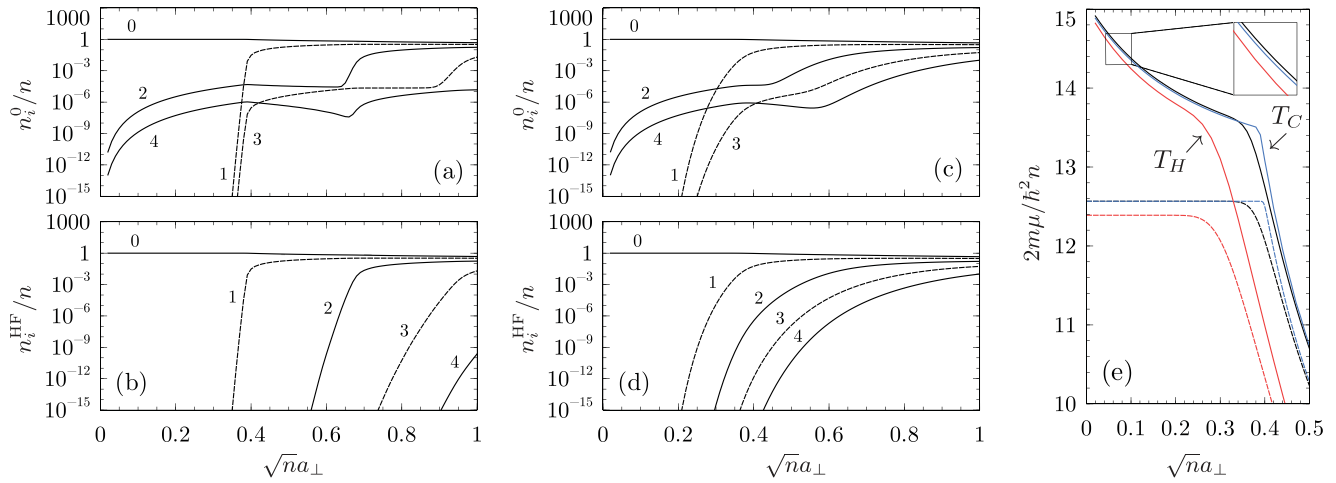

FIG. 3. (Color online) Subband mixing and renormalization of the chemical potential. Panels (a) and (b) show the fractional population of noninteracting subbands and Hartree-Fock subbands, respectively, as a function of transverse confinement width $a_\perp$ at constant dipolar interaction strength $r_d = 0.05$ and temperature $T = 0.1T^* \simeq 0.008T_F^{(0)}$. Panels (c) and (d) are the same quantities at a higher temperature $T = T^* \simeq 0.08T_F^{(0)}$. Panel (e) shows the chemical potential as a function of transverse confinement width $a_\perp$ at $T \equiv T_c = 0.1T^* \simeq 0.008T_F^{(0)}$ (solid blue), $T = 1.0T^* \simeq 0.08T_F^{(0)}$ (solid black), and $T \equiv T_H = 2.0T^* \simeq 0.16T_F^{(0)}$ (solid red). The dashed lines denote the chemical potential in the absence of interactions for comparison. Notice the nonmonotonic ordering of the chemical potential vs temperature in the inset (refer to text for discussion).

for the reduced DOS. At higher temperatures, once the states above the Fermi level are significantly populated, this effect is suppressed and a smaller chemical potential is required to keep the number of particles constant.

IV. PROBING THE INTERSUBBAND EXCITATIONS IN LATTICE MODULATION SPECTROSCOPY EXPERIMENTS

The single-particle and collective excitations of a strictly two-dimensional gas of polar fermionic molecules have been recently studied by several authors [22,34,37]. The two-dimensional gas corresponds to the single-subband limit of a quasi-two-dimensional gas and can be realized in strong traps. At zero tilt angle (i.e., when the dipoles are aligned perpendicular to the two-dimensional confining plane), the dipole-dipole interactions are effectively repulsive. The dipolar interactions are also short-range and regular in the long-wavelength limit. Therefore, such systems are expected to have the same qualitative properties as He-3, which is described well by Fermi liquid theory for neutral systems [56]. The elementary excitations of such systems consists of quasiparticle-like excitations and the zero sound.

Upon decreasing the strength of the trap, the gap between the subbands will be lowered and one enters the multisubband regime. In this regime, the intersubband elementary excitations must also be taken into account in addition to the intrasubband elementary excitations. These excitations also come in two flavors: quasiparticle-like excitations and *p-h* bound (or antibound) states known as excitons.

The intersubband excitations can be experimentally detected using the technique of lattice modulation spectroscopy [45–49] which was originally introduced and realized in cold atomic systems in order to study the Mott and superfluid phases of the Hubbard model. This method relies on the high controllability of the optical lattices which allows rapid modulation of the optical potential. Introducing a weak oscillatory modulation to the amplitude of the optical potential, one stimulates the transition of particles from lower subbands to higher subbands. The energy of the intersubband excitations must match the modulation frequency for the transition to occur. Therefore, one directly measures the excitation energy in such experiments and no tedious calibration of parameters is needed.

In order to measure the absorbed energy in modulation experiments, one allows the system to rethermalize after the modulation pulse. The new equilibrium state is then mapped to a noninteracting state by switching off the interactions adiabatically. For polar molecules, this can be done by slowly ramping down the polarizing dc electric field. Finally, the temperature (or kinetic energy) of the mapped noninteracting state is measured in a time-of-flight experiment. For weak modulation pulses, the change in the energy of the adiabatically mapped state is linearly proportional to the energy absorbed by the interacting system. One obtains the intersubband excitation spectrum of the system by repeating this procedure for a range of modulation frequencies. We refer to this procedure as energy-resolved measurements for brevity.

Another quantity which is often measured in modulation spectroscopy experiments is the change in the number of particles in each subband. We refer to such experiments as band-resolved measurements for brevity. In such experiments, rethermalization of the gas is avoided after the modulation pulse. Instead, the gas is allowed to expand ballistically quickly after the modulation pulse and the transverse momentum profile of the particles is measured. The particles are resolved into subbands by fitting the measured density profile to a weighted sum of the density profiles calculated from the transverse wave functions. Band-resolved measurements can be used to study the mechanism of energy absorption via intersubband processes.

A. Perturbative description of lattice modulation spectroscopy experiments

In this section, we describe a theoretical framework for predicting the results of modulation spectroscopy experiments of polar molecules. As mentioned in Sec. II, we are interested in the case of well-separated layers, where one can neglect the interlayer couplings and just focus on transitions within a single layer. For concreteness, we focus on the pancake at $z = 0$. Upon introducing the amplitude modulation, the optical potential takes the following time-dependent form:

$$\begin{aligned} V_{\rm lat}(z,t) &= [V_0 + V_1 f(t)] \sin^2(kz) \\ &\simeq \tfrac{1}{2} m\omega_{\rm trap}^2 z^2 + \xi f(t) z^2/a_\perp^2, \end{aligned} \tag{23}$$

where $\omega_{\rm trap} = k\sqrt{2V_0/m}$, $a_\perp = \sqrt{\hbar/(m\omega_{\rm trap})}$, $\xi = [\hbar\omega_{\rm trap}/(2V_0)]V_1$, and $f(t)$ is the shape of the amplitude modulation pulse. We have expanded the optical potential to quadratic order about its minimum at $z = 0$. The second-quantized form of the lattice modulation potential [i.e., the second term in Eq. (23)] can be written as

$$\hat{V}_{\rm mod}(t) = \xi f(t) \sum_{\mathbf{k},\alpha\beta} \mathbf{T}_{\alpha\beta} c^\dagger_{\mathbf{k}\alpha} c_{\mathbf{k}\beta}, \tag{24}$$

where $\mathbf{T}_{\alpha\beta} = a_\perp^{-2} \int dz \phi^*_\alpha(z) z^2 \phi_\beta(z)$. For a harmonic trap, $\mathbf{T}_{\alpha\beta}$ is given by

$$\begin{aligned} \mathbf{T}_{\alpha\beta} = \tfrac{1}{2}[&\sqrt{(\alpha+1)(\alpha+2)}\delta_{\alpha,\beta-2} \\ &+ \sqrt{\alpha(\alpha-1)}\delta_{\alpha,\beta+2} + (2\alpha+1)\delta_{\alpha\beta}]. \end{aligned} \tag{25}$$

It is easier for subsequent derivations to express the perturbation Hamiltonian in terms of Hartree-Fock fermion operators:

$$\hat{V}_{\rm mod}(t) = \xi f(t) \sum_{\mathbf{k},\alpha\beta} \tilde{\mathbf{T}}_{\alpha\beta}(\mathbf{k}) \tilde{n}_{\alpha\beta}(\mathbf{k}), \tag{26}$$

where

$$\begin{aligned} \tilde{n}_{\alpha\beta}(\mathbf{k}) &= \tilde{c}^\dagger_{\mathbf{k}\alpha} \tilde{c}_{\mathbf{k}\beta}, \\ \tilde{\mathbf{T}}_{\alpha\beta}(\mathbf{k}) &= \sum_{\alpha'\beta'} U_{\alpha'\alpha}(\mathbf{k}) U_{\beta'\beta}(\mathbf{k}) t_{\alpha'\beta'}. \end{aligned} \tag{27}$$

We note that both $\mathbf{T}_{\alpha\beta}$ and $\tilde{\mathbf{T}}_{\alpha\beta}$ are symmetric in the subband indices. It is clear from Eqs. (24) and (25) that the modulation perturbation stimulates an intersubband *p-h* excitation between subbands whose indices differ by ± 2. We have tacitly assumed in Eq. (23) that the amplitude

of the modulation pulse is low (i.e., $\xi \ll \hbar\omega_{\rm trap}$) and thus neglected the small anharmonic terms such as $\sim\cos(\omega t)z^4$, which stimulate transitions between subbands whose indices differ by ± 4.

For low-amplitude modulations and short modulation pulse durations, the disturbance in the equilibrium state of the system is negligible and we can treat the modulation pulse in perturbation theory. In the first-order approximation, the response of the system to an oscillatory external field is also purely oscillatory and yields no steady current on average. Thus, one needs to consider processes that are at least second order in the external fields in order to describe spectroscopic probes such as energy absorption and interband transitions in lattice modulation experiments.

We focus on energy-resolved measurements first. A straightforward calculation yields the following expression for the energy absorption rate, $\dot{E}(t) \equiv \partial_t \mathrm{Tr}[\hat{\rho}(t)\hat{H}]$, in second-order perturbation theory:

$$\begin{aligned}\dot{E}(t) &= 2\mathrm{Re}\int_{-\infty t} dt' \langle \hat{V}_{\rm mod}(t)\hat{H}\hat{V}_{\rm mod}(t') - \hat{H}\hat{V}_{\rm mod}(t)\hat{V}_{\rm mod}(t')\rangle \\ &= i\xi^2 f(t)\int_{-\infty}^{\infty} dt' f(t')\partial_t \mathcal{T}(t-t'), \end{aligned} \tag{28}$$

where

$$\mathcal{T}(t) = \sum_{\mathbf{k}_1,\alpha\beta}\sum_{\mathbf{k}_2,\gamma\lambda} \mathcal{T}_{\alpha\beta;\gamma\lambda}(\mathbf{k}_1,\mathbf{k}_2,t) \tag{29}$$

and

$$\mathcal{T}_{\alpha\beta;\gamma\lambda}(\mathbf{k}_1,\mathbf{k}_2,t) = \tilde{\mathbf{T}}_{\alpha\beta}(\mathbf{k}_1)\tilde{\mathbf{T}}_{\gamma\lambda}(\mathbf{k}_2)\tilde{\Pi}^R_{\alpha\beta;\gamma\lambda}(\mathbf{k}_1,\mathbf{k}_2;t), \tag{30}$$

in which $\tilde{\Pi}^R_{\alpha\beta;\gamma\lambda}(\mathbf{k}_1,\mathbf{k}_2;t)$ is the retarded intersubband polarization insertion

$$\tilde{\Pi}^R_{\alpha\beta;\gamma\lambda}(\mathbf{k}_1,\mathbf{k}_2;t) = -i\theta(t)\mathrm{Tr}\{\hat{\rho}_0[\tilde{n}_{\beta\alpha}(\mathbf{k}_1,t),\tilde{n}_{\gamma\lambda}(\mathbf{k}_2,0)]\}. \tag{31}$$

In the experiments, the lattice modulation pulse is switched on and off smoothly. For concreteness, we assume an exponentially switched-on pulse

$$f(t) = e^{-\eta|t|}\cos(\Omega t), \tag{32}$$

where η is the switching rate and Ω is the frequency of the ac modulation. We chose the exponentially switched-on pulse (shown in Fig. 5) since it yields simple and transparent analytical expressions. It is shown in Appendix C that the energy absorption rate for such a pulse is given by

$$\dot{E}|_{\Omega,\eta} = -\frac{\xi^2}{4}\Omega\mathrm{Im}[\mathcal{T}(\Omega+i\eta)] + O\big(\hbar\xi^2\eta\omega_{\rm trap}^{-1}\big). \tag{33}$$

Note that, in light of Eqs. (29) and (30), $\mathcal{T}(\omega)$, the Fourier transform of $\mathcal{T}(t)$, can be identified as the self-energy correction of the optical lattice photons with energy $\hbar\omega$ coupled to the fermionic molecules. Thus, Eq. (33) can be simply interpreted as the energy of the absorbed photons multiplied by their decay rate (i.e., the imaginary part of their self-energy).

It is evident from Eq. (29) that the fundamental quantity to be evaluated is $\tilde{\Pi}^R_{\alpha\beta;\gamma\lambda}(\mathbf{k}_1,\mathbf{k}_2;t)$; namely, the dynamical intersubband polarization insertion with zero net momentum transfer. Except for a few exactly solvable models, the polarization insertion can only be evaluated approximately by summing certain classes of diagrams. A realistic many-body approximation is expected to satisfy particle number, energy, and momentum conservation laws [50]. The conservation laws can often be expressed as sum rules for correlation functions. We discuss the sum rules relevant to the present problem in Sec. IV C 3 and utilize them to check the consistency of the obtained numerical results.

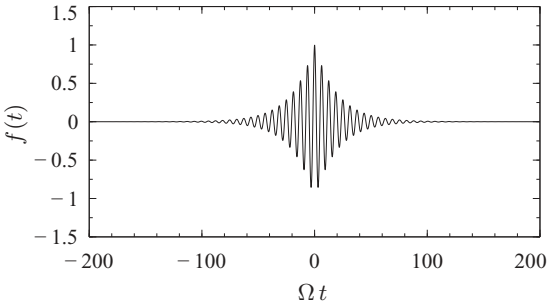

FIG. 5. Plot of ac pulse for $\eta/\Omega = 0.05$. The band-resolved measurement is done at $t = 0$.

B. Energy absorption and intersubband transition rates in time-dependent Hartree-Fock approximation

We evaluate the polarization insertion in the conserving time-dependent Hartree-Fock (TDHF) approximation [50], also known as the generalized random phase approximation (GRPA) [56] or the random phase approximation with exchange (RPAE) [57]. TDHF is considered the simplest conserving many-body approximation that respects the quantum statistics of the particles. Once the polarization insertion matrix elements are found, the energy absorption rate can be easily evaluated using Eqs. (29), (30), and (33). We carry out the diagrammatic calculations in the imaginary-time formalism. The retarded polarization appearing in Eq. (30) can be found by the standard procedure of analytical continuation of the Matsubara frequency to the upper complex frequency half-plane:

$$\tilde{\Pi}_{\alpha\beta;\gamma\lambda}(\mathbf{k}_1,\mathbf{k}_2;\Omega) = \tilde{\Pi}_{\alpha\beta;\gamma\lambda}(\mathbf{k}_1,\mathbf{k}_2;i\nu_n\to\Omega). \tag{34}$$

Evaluating polarization diagrams in the TDHF approximation amounts to summing the direct and exchange scatterings between the p-h pairs to all orders in each p-h loop. In other words, the full polarization diagram is the sum of all ring diagrams with ladder-like vertex corrections [50]. The successive iterations of the following Bethe-Salpeter equation generates all such contributions:

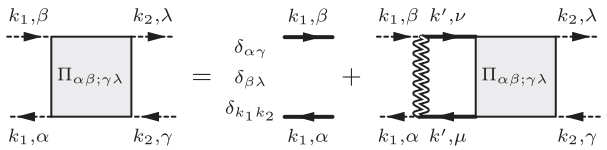

(35)

where the double zigzag line represents the combined direct and exchange interaction between Hartree-Fock quasiparticles:

$$\tilde{\mathcal{U}}^{(\mathrm{d+e})}_{\alpha\beta;\mu\nu}(\mathbf{k},\mathbf{k}') =$$

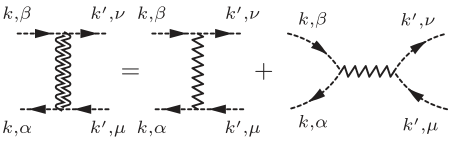

$$= \tilde{\mathcal{V}}_{\nu\beta;\alpha\mu}(\mathbf{k},\mathbf{k}'-\mathbf{k}) - \tilde{\mathcal{V}}_{\alpha\beta;\nu\mu}(\mathbf{k},\mathbf{k}',0). \tag{36}$$

The negative sign of the direct interaction is due to the extra fermion loop it introduces. The diagrammatic Eq. (35) yields

$$\tilde{\Pi}_{\alpha\beta;\gamma\lambda}(\bar{k}_1,\bar{k}_2;i\nu_n) = \tilde{\mathcal{G}}_\alpha(\mathbf{k}_1,i\omega_{n_1}+i\nu_n)\tilde{\mathcal{G}}_\beta(\mathbf{k}_1,i\omega_{n_2}) \times\Bigg[\delta_{\alpha\gamma}\delta_{\beta\lambda}\delta_{\mathbf{k}_1\mathbf{k}_2} - \frac{1}{\beta}\sum_{i\omega'_n}\int\frac{\mathrm{d}^2\mathbf{k}'}{(2\pi)^2} \times\tilde{\mathcal{U}}^{(\mathrm{d+e})}_{\alpha\beta;\mu\nu}(\mathbf{k}_1,\mathbf{k}')\tilde{\Pi}_{\mu\nu;\gamma\lambda}(\bar{k}',\bar{k}_2;i\nu_n)\Bigg], \tag{37}$$

where $\bar{k}_1 = (\mathbf{k}_1, i\omega_{n_1})$, $\bar{k}_2 = (\mathbf{k}_2, i\omega_{n_2})$, and $\bar{k}' = (\mathbf{k}', i\omega'_n)$. We note that, if we had formulated the problem in the noninteracting basis, the Green's functions would have been nondiagonal in the subband indices and the resulting integral equation would have had additional intermediate subband index summations.

Summing both sides of Eq. (37) over the Matsubara frequencies $i\omega_{n_1}$ and $i\omega_{n_2}$ and analytically continuing $i\nu_n \to \Omega$, with Ω being an arbitrary point in the upper complex half-plane, we get

$$\tilde{\Pi}_{\alpha\beta;\gamma\lambda}(\mathbf{k}_1,\mathbf{k}_2;\Omega) = \tilde{\Pi}^{(0)}_{\alpha\beta}(\mathbf{k}_1;\Omega)\Bigg[\delta_{\alpha\gamma}\delta_{\beta\lambda}\delta_{\mathbf{k}_1\mathbf{k}_2} - \int\frac{\mathrm{d}^2\mathbf{k}'}{(2\pi)^2} \times\tilde{\mathcal{U}}^{(\mathrm{d+e})}_{\alpha\beta;\mu\nu}(\mathbf{k}_1,\mathbf{k}')\tilde{\Pi}_{\mu\nu;\gamma\lambda}(\mathbf{k}',\mathbf{k}_2;\Omega)\Bigg], \tag{38}$$

where $\tilde{\Pi}^{(0)}_{\alpha\beta}(\mathbf{k};\Omega)$, the bare intersubband polarization with zero net momentum transfer, is defined as

$$\tilde{\Pi}^{(0)}_{\alpha\beta}(\mathbf{k};\Omega) = \frac{1}{\beta}\sum_{i\omega_n}\tilde{\mathcal{G}}_\alpha(\mathbf{k};i\omega_n+i\nu_n)\tilde{\mathcal{G}}_\beta(\mathbf{k};i\omega_n)\Big|_{i\nu_n\to\Omega} = \frac{n_\beta(\mathbf{k})-n_\alpha(\mathbf{k})}{\Omega+\tilde{\xi}_\beta(\mathbf{k})-\tilde{\xi}_\alpha(\mathbf{k})}. \tag{39}$$

The poles of $\tilde{\Pi}^{(0)}_{\alpha\beta}(\mathbf{k};\Omega)$ correspond to $\beta\to\alpha$ p-h excitation energies.

Equation (38) is an integral equation for the intersubband polarization. However, it is more suitable for our purpose to formulate an integral equation for the following auxiliary function, in which some of the summations appearing in Eq. (29) are already carried out:

$$\tilde{h}_{\alpha\beta}(\mathbf{k}_1;\Omega) = \frac{\sum_{\mathbf{k}_2,\gamma\lambda}\tilde{\Pi}_{\alpha\beta;\gamma\lambda}(\mathbf{k}_1,\mathbf{k}_2;\Omega)\tilde{\mathbf{T}}_{\gamma\lambda}(\mathbf{k}_2)}{\tilde{\Pi}^{(0)}_{\alpha\beta}(\mathbf{k}_1;\Omega)}. \tag{40}$$

Using Eq. (38), one easily finds

$$\tilde{h}_{\alpha\beta}(\mathbf{k}_1;\Omega) = \tilde{\mathbf{T}}_{\alpha\beta}(\mathbf{k}_1) - \int\frac{d^2\mathbf{k}'}{(2\pi)^2}\tilde{\mathcal{U}}^{(\mathrm{d+e})}_{\alpha\beta;\mu\nu}(\mathbf{k}_1,\mathbf{k}') \times\tilde{\Pi}^{(0)}_{\mu\nu}(\mathbf{k}';\Omega)\tilde{h}_{\mu\nu}(\mathbf{k}';\Omega). \tag{41}$$

Iterating the above integral equation,

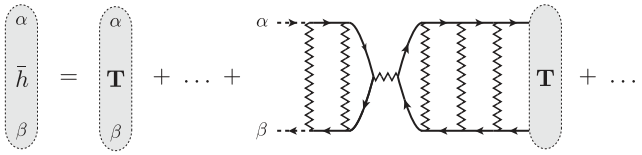

one identifies $\tilde{h}_{\alpha\beta}$ as the effective intersubband transition matrix including the interaction effects. The presence of p-h scatterings to all orders suggests that $\tilde{h}_{\alpha\beta}(\mathbf{k};\Omega)$ will have poles at excitonic energies. Note that, in contrast to Eq. (38), the bare polarizations (which have integrable singularities) appear under integrals in the above equation. Therefore, provided that its Fredholm determinant is nonvanishing, Eq. (41) yields smooth solutions. The Fredholm determinant, however, may vanish for an isolated set of frequencies, corresponding to the excitons. We use this criteria for locating the excitons.

Once $h_{\alpha\beta}(\mathbf{k};\Omega)$ is found, $\mathcal{T}(\Omega)$ can be readily evaluated using Eq. (40):

$$\mathcal{T}(\Omega) = \sum_{\alpha\beta}\sum_{\mathbf{k}_1}\tilde{\mathbf{T}}_{\alpha\beta}(\mathbf{k}_1)\tilde{\Pi}^{(0)}_{\alpha\beta}(\mathbf{k}_1;\Omega)\tilde{h}_{\alpha\beta}(\mathbf{k}_1;\Omega). \tag{42}$$

The numerical procedure used to solve the integral equation for $\tilde{h}_{\alpha\beta}$ is described in detail in Appendix E.

In the TDHF approximation, the excitons that lie outside of p-h continua are undamped and have infinitely long lifetimes. Therefore, they will appear as poles just below the real frequency axis in $\tilde{h}_{\alpha\beta}(\mathbf{k};\Omega)$ and $\mathcal{T}(\Omega)$. According to Eq. (33), the undamped excitons yield sharp Dirac-delta-like peaks in the energy absorption spectrum in the adiabatic pulse switching limit ($\eta\to 0$). The spectral weight of an exciton can be found using the analyticity of $\mathcal{T}(\omega)$ in the upper complex frequency half-plane. Assuming that that $\mathcal{T}(\omega)$ is singular at $\omega = \omega_0 - i0^+$, one can find the spectral weight associated to it using the Kramers-Kronig relations:

$$W|_{\omega=\omega_0} = \frac{\pi\xi^2}{4}\omega_0\lim_{\omega\to\omega_0}\{(\omega-\omega_0)\mathrm{Re}[\mathcal{T}(\omega)]\}. \tag{43}$$

In the remainder of this section, we address the subtler problem of evaluating the intersubband transition rates. The subtlety originates from the fact that the population of each subband is not conserved separately by the microscopic Hamiltonian. The presence of intersubband interaction matrix elements such as $\mathcal{V}_{\gamma\alpha;\gamma\beta}$ implies that $[\hat{N}_\gamma,\hat{H}]\neq 0$, where $\hat{N}_\gamma$ is the total number operator of particles in subband γ. We note that this result holds for Hartree-Fock number operators as well. As a consequence, the intersubband excitations generated by the lattice modulation term are subject to nonequilibrium dynamics as the system evolves and the rates cannot be evaluated using linear response theory. Ultimately, one needs to utilize the Schwinger-Keldysh formalism and nonequilibrium Green's functions in order to calculate the transition rates. We note that this additional difficulty is not present in theories in which the number of each species is

conserved separately. In those cases, the transition rates can be evaluated using the equilibrium formalism in second-order perturbation theory [58].

We quote the final result of the nonequilibrium analysis and leave the technical details for future works. In brief, our strategy is to solve the nonequilibrium Dyson's equation up to second order in the external field. The intersubband transition rates can be extracted from the second-order corrections to the nonequilibrium Green's functions. For the exponentially switched-on pulse, we find the total number of particles transferred from the Hartree-Fock subband α to β for times $t \leqslant 0$ to be

$$\Delta\tilde{N}_{\alpha\to\beta}(t)|_{t\leqslant 0} = \frac{e^{-2\eta|t|}}{4\eta}|\tilde{h}_{\beta\alpha}(\Omega+i\eta)|^2\mathrm{Im}\big[\tilde{\Pi}^{(0)}_{\alpha\beta}(\Omega+i\eta)\big]. \tag{44}$$

We have neglected the oscillatory terms in the above equation. Such contributions are the second harmonics of the external ac field which naturally arise in second-order perturbation theory. In the limit $\eta/\Omega \ll 1$, the oscillatory terms are much smaller than the retained term. Moreover, they yield no steady transition current on average due to their oscillatory nature.

The effective duration of the exponentially switched-on pulse from $t=-\infty$ to $t=0$, when the measurement takes place, is $\Delta t \sim \eta^{-1}$. We define the effective intersubband transition rate as

$$\tilde{\mathcal{R}}_{\alpha\to\beta} \equiv \eta\Delta\tilde{N}_{\alpha\to\beta}(0). \tag{45}$$

For weakly interacting systems, subband hybridization is a negligible effect (see Fig. 3; the fractional hybridization is $\sim 10^{-6}$ for $r_d = 0.05$) and the transition rates between Hartree-Fock subbands are virtually the same as the transition rates between the noninteracting subbands; that is, $\Delta\tilde{N}_{\alpha\to\beta}(t) \approx \Delta N_{\alpha\to\beta}(t)$ and $\tilde{\mathcal{R}}_{\alpha\to\beta} \approx \mathcal{R}_{\alpha\to\beta}$.

We conclude our discussion of the TDHF approximation with a brief remark on its reliability in the context of modulation experiments. Apart from the absence of correlation effect that restricts its application to weakly interacting systems, a major shortcoming of the TDHF approximation is the absence of collision integrals that describe relaxation processes. The reliability of the time evolution of an operator in the TDHF approximation can thus be judged based on its commutation with the Hamiltonian. We refer to operators that commute with the Hamiltonian in the absence of the external perturbation as conserved operators. The nonconserved operators are defined likewise.

Since the expectation value of conserved operators remains intact during relaxation processes, the time evolution of such operators is essentially unaffected by the lack of collision integrals. Therefore, we expect that the TDHF prediction for the energy absorption rate (which is the expectation value of the Hamiltonian, a manifestly conserved operator) to be reliable. In particular, the quality of this prediction is expected to be indifferent to the duration of the modulation pulse, provided that its amplitude and power are not too large.

On the other hand, relaxation processes play an important role in the time evolution of nonconserved quantities, such as the population of individual subbands. In particular, studying the time evolution of such operators must be avoided in the limit of adiabatically switched pulses, where the relaxation processes play a central role. Generally, one must make sure that the lifetime of excitations is longer than the pulse duration in order to justify the absence of relaxation processes in the theory. For the exponentially switched-on pulse of Eq. (32), this condition leads to the following criteria:

$$\left\langle\Gamma^{\mathrm{rel}}_{\alpha}\right\rangle < 2\eta \quad (\text{for all } \alpha), \tag{46}$$

where $\langle\Gamma^{\mathrm{rel}}_{\alpha}\rangle$ is the average relaxation rate of an excitation in subband α. An estimate of $\langle\Gamma^{\mathrm{rel}}_{2}\rangle$ for quasiparticle-like excitations is provided in Appendix D. We will use Eq. (46) and the results of Appendix D in order to choose an appropriate value for η. We note that, in experiments with reactive polar molecules, another constraint on the pulse duration results from the reduced lifetime of molecules in the higher subbands. In practice, η must be chosen to be larger than both the relaxation rate and the molecule loss rate.

C. Results

In this section, we present the results obtained by evaluating Eqs. (33) and (44) numerically. We keep the first five subbands in the numerical calculations. The results are given in terms of the following dimensionless and intensive quantities:

$$\begin{aligned} \dot{\varepsilon} &\equiv (2\hbar N^{-1}\xi^{-2})\dot{E}, \\ w &\equiv \left(2\hbar N^{-1}\xi^{-2}\omega_{\mathrm{trap}}^{-1}\right)W, \\ r_{\alpha\to\beta} &\equiv (2\hbar^2 N^{-1}\xi^{-2})\Omega\mathcal{R}_{\alpha\to\beta}, \\ \bar{\Omega} &\equiv \Omega/\omega_{\mathrm{trap}}. \end{aligned} \tag{47}$$

Based on the remarks mentioned at the end of the previous section, one expects the energy absorption spectrum obtained in experiments done at a finite switching rate to be essentially a broadened version of those obtained in the adiabatic limit. In fact, the appearance of $\mathcal{T}(\Omega+i\eta)$ in Eq. (33) and the analyticity of $\mathcal{T}(\omega)$ in the upper complex frequency half-plane is a rigorous justification of this claim. In light of this observation, we have evaluated the energy absorption rates in the adiabatic limit for the clarity of presentation. In this limit, the excitonic peaks will be Dirac-delta-like and one can easily distinguish excitons from the p-h continua.

1. Energy absorption rates

We start with the simpler case of a strong trap at low temperatures where only the lowest subband is populated. Figure 6 shows the energy absorption spectrum for a range of weak dipolar interactions $r_d = 0.001, 0.005, 0.010, \ldots, 0.050$ at a fixed transverse confinement width $\sqrt{n}a_\perp = 0.2$ and temperature $T = 0.1T^* \simeq 0.008T_F^{(0)}$. We find that the spectrum consists of a single p-h continuum, corresponding to $0\to 2$ transitions, and a single exciton. The energy of the exciton lies above the p-h continuum and, therefore, is an antibound p-h pair. The antibinding nature of the excitonic mode is a consequence of the anisotropic dipole-dipole interactions. The exciton captures $99.74\% \pm 0.01\%$ of the spectral weight, leaving only $0.26\% \pm 0.01\%$ for the continuum. These ratios were found to be independent of r_d in the studied range, although they may depend on $a_\perp$ and T.

Figure 7 shows the energy absorption spectrum for various temperatures in the range $0.04 < T/T_F^{(0)} < 1.60$ at a fixed

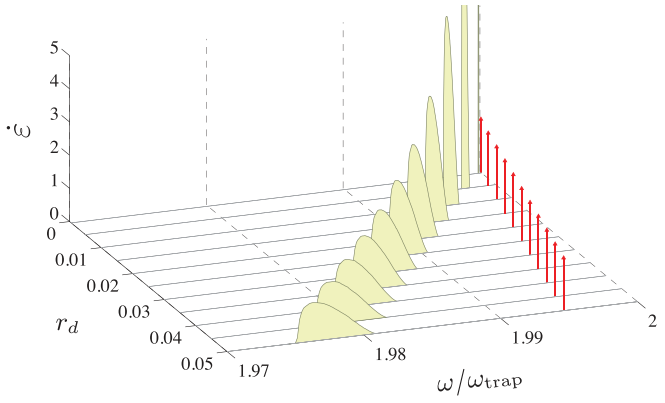

FIG. 6. (Color online) Energy absorption rate plots for various dipolar interaction strengths at fixed $\sqrt{n}a_\perp = 0.2$ and $T = 0.1T^* \simeq 0.008T_F^{(0)}$. In all of the cases shown, the spectrum consists of a single p-h excitation continuum (yellow shaded continuum) and a single antibound exciton (red spikes). The exciton captures 99.74% of the spectral weight for the range of r_d shown in the figure.

transverse confinement width $\sqrt{n}a_\perp = 0.2$ and dipolar interaction strength $r_d = 0.05$. We found that, at low temperatures, the spectrum consists of a single exciton and a single p-h continuum corresponding to $0 \to 2$ transitions (light, yellow shaded continua). As the temperature is increased, the spectral weight of the excitonic mode drops slightly from $99.74\% \pm 0.01\%$ to $99.67\% \pm 0.01\%$. At this point, the p-h continuum associated to $1 \to 3$ transitions (dark blue shade) becomes visible due to thermal population of the first-excited subband. The exciton also merges into the $1 \to 3$ continuum. At higher temperatures, more p-h continua appear continuously due to thermal population of higher subbands. We also notice that the $1 \to 3$ exciton, which initially appears on the edge of the $1 \to 3$ continuum (the peak at the end of

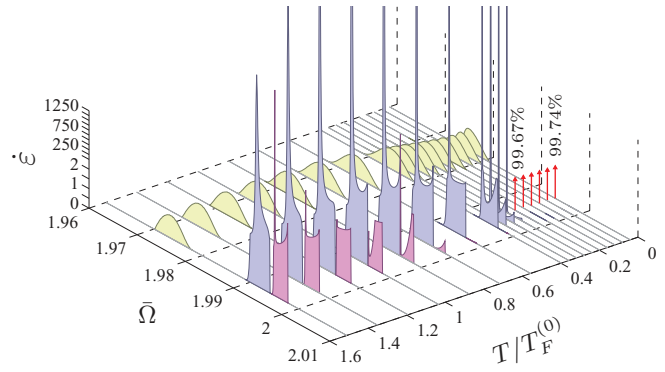

FIG. 7. (Color online) Energy absorption rate plots for various temperatures at fixed $\sqrt{n}a_\perp = 0.2$ and $r_d = 0.05$ (achievable in the current experiments of the group at JILA). The excitons appear as red spikes and their fractional spectral weights are shown above them. At low temperatures, the spectrum consists of a single p-h continuum corresponding to $0 \to 2$ transitions (light yellow shaded continua) and a single exciton (red spikes). At higher temperatures, more p-h excitation continua appear continuously due to thermal occupation of higher subbands. The (dark) blue and (darker) violet shaded continua correspond to $1 \to 3$ and $2 \to 4$ transitions respectively. The excitonic modes capture more than 99% of the spectral weight, whether they are outside or inside p-h continua.

the $1 \to 3$ continuum, visible for $T/T_F^{(0)} \simeq 0.4$ to ~ 1.0), moves out of the continuum and merges into the $2 \to 4$ continuum (visible for $T/T_F^{(0)} \gtrsim 1.0$). We expect that all of the excitons and continua converge to a single peak at $\omega = 2\omega_{\rm trap}$ at temperatures well above quantum degeneracy, where all interaction effects are masked due to thermal fluctuations. The shift of $0 \to 2$ continuum toward $\omega = 2\omega_{\rm trap}$ and its shrinking for $T > T_F^{(0)}$ agrees with this expectation.

Figure 8 shows the energy absorption spectrum for various transverse confinement widths at a fixed dipolar interaction strength $r_d = 0.05$ for two different temperatures $T = 0.1T^* \simeq 0.008T_F^{(0)}$ [Fig. 8(a)] and $T = 10T^* \simeq 0.8T_F^{(0)}$ [Fig. 8(b)]. The low- and high-temperature results have strikingly similar features. For strong traps (small $a_\perp$), the spectrum consists of a single exciton and a single p-h continuum. Like before, the exciton captures more than 99% of the spectral weight. Upon relaxing the trap (increasing $a_\perp$), the energy gap between the subbands is reduced and the higher subbands will be populated, resulting in the appearance of more p-h continua and excitonic modes associated to each continuum. In the low-temperature case [Fig. 8(a)], the excitons lie outside of continua in most of the plots while, at higher temperatures, the continua are broadened and the excitons lie inside the continua in most cases. Had we included higher subbands in the calculations, the bare exciton appearing in Fig. 8(b) for $\sqrt{n}a_\perp > 0.3$ would have appeared inside the $3 \to 5$ p-h continuum.

We find that, as soon as a new exciton appears (upon increasing $a_\perp$), it continuously captures the spectral weight of the exciton below it as the trap is relaxed further. Thus, one may question the nature of excitons in multisubband systems; that is, whether they are associated to certain intersubband transitions or inherit the properties of the previously appeared excitons as they absorb their spectral weight. We address this question in the next section where we discuss intersubband transition rates.

Another interesting finding is the appearance of the Fano line-shape [59] in parts of the spectrum. This phenomenon is most easily noticeable in the $1 \to 3$ continua for $\sqrt{n}a_\perp > 0.34$ in Fig. 8(b). The missing spectral weight inside the continuum is associated to the interference of the p-h excitations and the excitonic mode just above it.

It is worthy of mention that, despite the fact that all of the results presented so far belong to the weakly interacting regime ($r_d \leqslant 0.05$), one finds that the presence of interactions dramatically modifies the intersubband excitation spectrum. In the absence of interactions, all of the structures shown in Figs. 6, 7, and 8 disappear, leaving a single peak at $\omega = 2\omega_{\rm trap}$ (see Fig. 1).

2. *Intersubband transition rates*

Motivated by band-resolved spectroscopy experiments and also in order to elucidate the nature of excitons, we evaluate the intersubband transition rates in this section. According to the remarks at the end of Sec. IV A [see Eq. (46)] and the estimates obtained in Appendix D for the quasiparticle relaxation rate, we choose $\eta = 0.01\hbar n/(2m)$. This choice guarantees the modulation pulse duration to be smaller than the lifetime of most intersubband excitations and thus justifies the use of the TDHF approximation.

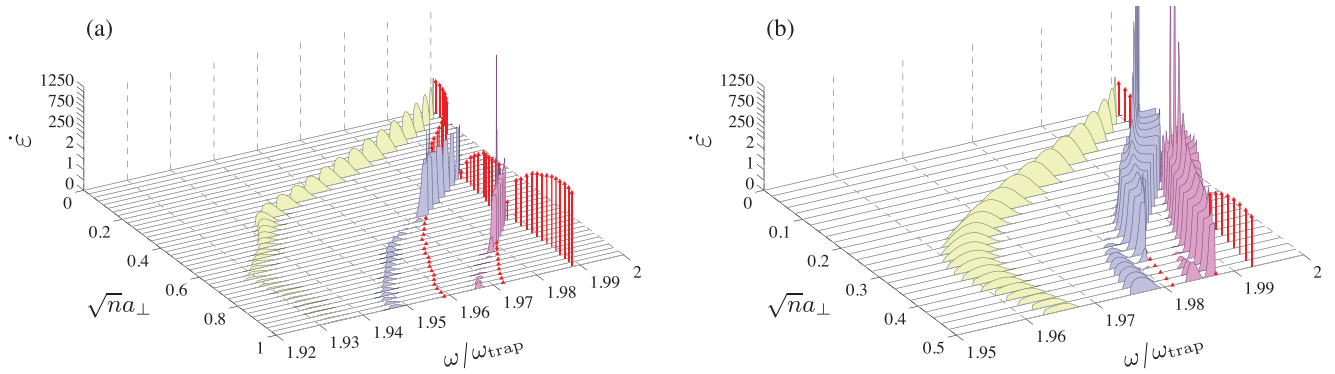

FIG. 8. (Color online) Energy absorption rate plots for various transverse confinement widths at fixed $r_d = 0.05$. (a) $T = 0.1T^* \simeq 0.008T_F^{(0)}$, (b) $T = 10T^* \simeq 0.8T_F^{(0)}$. The excitons appear as red spikes. For strong transverse confinements (small $a_\perp$), the spectrum consists of a single p-h continuum corresponding to $0 \to 2$ transitions (light yellow shaded continua) and a single exciton (red spikes). For weaker transverse confinements (larger $a_\perp$), more p-h excitation continua appear continuously due to the reduced energy gap between the subbands, corresponding to transitions $1 \to 3$ (dark, blue), $2 \to 4$ (darker, violet), etc. The length of the spikes indicate their dimensionless spectral weight w. The excitonic modes capture more than 99% of the spectral weight, whether they are outside or inside p-h continua.

Figure 9 shows the energy absorption rate along with different intersubband transition rates for three transverse confinement widths at $T = 0.1T^* \simeq 0.008T_F^{(0)}$. The topmost plots are slices of Fig. 8(a), which are broadened due to the finite switching-on rate. The energy absorption rates in the adiabatic switching limit are also shown for comparison. Note that we have chosen different scales along the vertical axis for clarity of presentation.

For $\sqrt{n}a_\perp = 0.30$ [Figs. 9(a1) and 9(a2)], the spectrum consists of a single p-h continuum and an exciton. The only nonvanishing intersubband-transition channel is $0 \to 2$. For $\sqrt{n}a_\perp = 0.45$ [Figs. 9(b1), 9(b2), and 9(b3)], the spectrum consists of two p-h continua and two excitons. We find that the excitons have a mixed nature in this case; that is, although the first and the second excitons are mainly composed of $0 \to 2$ and $1 \to 3$ p-h pairs, each has a considerable contribution from the other p-h pairs. For $\sqrt{n}a_\perp = 0.54$ [Figs. 9(c1), 9(c2), and 9(c3)], one finds that the spectral weight of the first exciton is reduced and the second exciton dominates. The energy absorption is mainly due to $1 \to 3$ transitions in this case.

Figure 10 shows the same quantities as Fig. 9 but at a higher temperature $T = 10T^* \simeq 0.8T_F^{(0)}$. For $\sqrt{n}a_\perp = 0.05$ [Figs. 10(a1) and 10(a2)], the spectrum consists of a single p-h continuum and an exciton, both of which are associated to $0 \to 2$ transitions. For $\sqrt{n}a_\perp = 0.16$ [Figs. 10(b1), 10(b2), and 10(b3)], the spectrum consists of two p-h continua and one visible exciton which lies inside the second continuum. The exciton is a mixture of both $0 \to 2$ and $1 \to 3$ p-h pairs. For $\sqrt{n}a_\perp = 0.28$ [Figs. 10(c1)–10(c4)], one finds more continua and excitons. Again, the excitons are mixtures of different p-h pairs.

Another interesting finding is the significantly reduced spectral weight between the two excitons in the $r_{0\to2}$ plots [see Figs. 9(b2), 9(c2), and 10(c2)]. This phenomenon is an

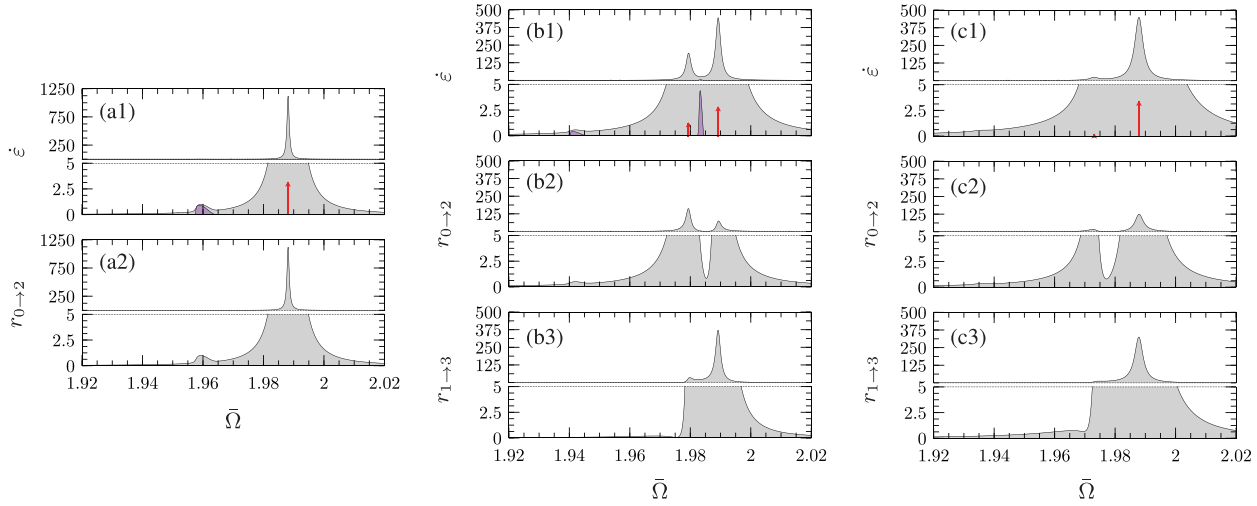

FIG. 9. (Color online) Energy absorption rates and intersubband transition rates for various transverse confinement widths at a fixed dipolar interaction strength $r_d = 0.05$ and temperature $T = 0.1T^* \simeq 0.008T_F^{(0)}$. The gray shaded plots correspond to quantities evaluated at a finite pulse switching rate of $\eta = 0.01\hbar n/(2m)$. The spikes (excitons) and darker continua correspond to the adiabatic switching limit and are shown for comparison. The red spikes correspond to excitons lying outside of p-h continua in the adiabatic limit. The length of the spikes indicate their dimensionless spectral weight w. Panels (a1) and (a2): $\sqrt{n}a_\perp = 0.30$. Panels (b1)–(b3): $\sqrt{n}a_\perp = 0.45$. Panels (c1)–(c3): $\sqrt{n}a_\perp = 0.58$.

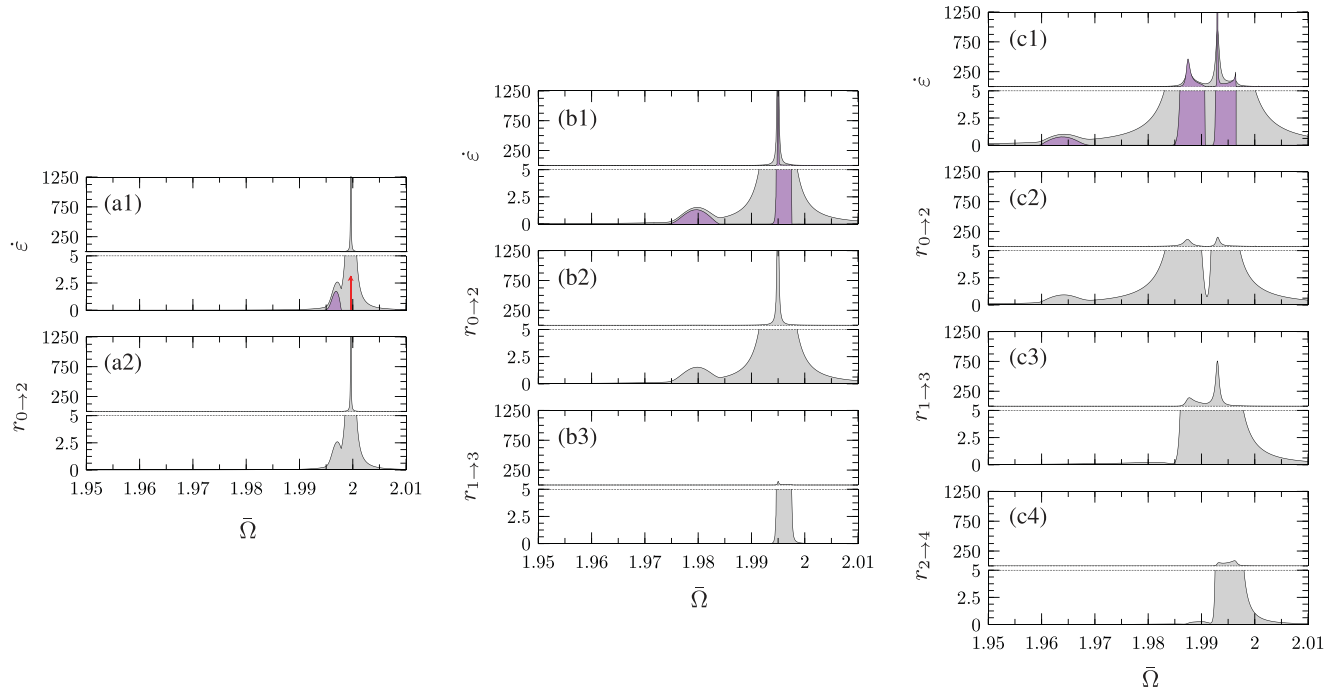

FIG. 10. (Color online) Energy absorption rates and intersubband transition rates for various transverse confinement widths at a fixed dipolar interaction strength $r_d = 0.05$ and temperature $T = 10T^* \simeq 0.8T_F^{(0)}$. The gray shaded plots correspond to quantities evaluated at a finite pulse switching rate of $\eta = 0.01\hbar n/(2m)$. The spikes (excitons) and darker continua correspond to the adiabatic switching limit and are shown for comparison. The red spikes correspond to excitons lying outside of p-h continua in the adiabatic limit. The length of the spikes indicate their dimensionless spectral weight w. Panels (a1) and (a2): $\sqrt{n}a_\perp = 0.05$. Panels (b1)–(b3): $\sqrt{n}a_\perp = 0.13$. Panels (c1)–(c3): $\sqrt{n}a_\perp = 0.28$.

example of Fano interference between the excitons and has also been previously studied in semiconductor quantum wells [60].

3. *Numerical check of sum rules*

Realistic many-body approximations are expected to yield response functions that abide by the conservation laws resulting from symmetries of the Hamiltonian. The conservation laws can often be expressed in the form of sum rules for correlation functions. The TDHF approximation belongs to the class of conserving approximations and is expected to satisfy such sum rules rigorously. These rules can thus be used to check the consistency of the numerical calculations.

The sum rule associated to particle number conservation, known as the longitudinal f-sum rule, can be most easily derived by by evaluating the quantity $\langle[[H,\rho(\mathbf{q})],\rho(-\mathbf{q})]\rangle$ in two ways (i.e., directly using commutation relations and using the Källén-Lehmann representation [58]). Here, $\rho(\mathbf{q}) = \sum_{\mathbf{k},\alpha} c^\dagger_{\mathbf{k},\alpha} c_{\mathbf{k}+\mathbf{q},\alpha}$. The final result is easily found to be

$$\int_0^\infty \frac{d\Omega}{\pi}\Omega\mathrm{Im}\left[\sum_{\mathbf{k}_1,\mathbf{k}_2}\Pi^R_{\alpha\alpha;\beta\beta}(\mathbf{k}_1,\mathbf{k}_2;\mathbf{q},\Omega)\right] = -\frac{|\mathbf{q}|^2}{2m}N, \quad (48)$$

where N is the total number of particles in all subbands. Since the lattice modulation pulse only creates p-h excitations with zero center-of-mass momentum, we only needed to calculate polarization parts at $\mathbf{q} = 0$ [see Eqs. (30) and (33)]. The f-sum rule is trivially satisfied in the TDHF approximation in this limit: the right-hand side of the above equation vanishes and, investigating Eqs. (38) and (39), one finds $\lim_{\mathbf{q}\to0}\Pi^R_{\alpha\alpha;\beta\beta}(\mathbf{k}_1,\mathbf{k}_2;\mathbf{q},\Omega) = 0$ at finite Ω. The ambiguity at $\Omega = 0$ is not problematic due to the presence of an extra factor of Ω in the integrand of the above equation.

A sum rule associated to the conservation of energy in modulation experiments can be found by evaluating $\langle[[H,\hat{V}_m],\hat{V}_m]\rangle$ in the two ways mentioned above, where $\hat{V}_m = \sum_{\alpha\beta}\sum_{\mathbf{k}}\mathbf{T}_{\alpha\beta}c^\dagger_{\mathbf{k},\alpha}c_{\mathbf{k},\beta}$. A straightforward calculation yields

$$\int_0^\infty \frac{d\Omega}{\pi}\Omega\mathrm{Im}[\mathcal{T}(\Omega)] = -\frac{1}{2}\sum_{\alpha\beta\gamma}\Delta_{\alpha\beta}\mathbf{T}_{\alpha\beta}(\mathbf{T}_{\alpha\gamma}N_{\gamma\beta} - \mathbf{T}_{\beta\gamma}N_{\gamma\alpha}), \quad (49)$$

where $\Delta_{\alpha\beta} = \epsilon_\alpha - \epsilon_\beta$ is the noninteracting band gap [see Eq. (3)] and $N_{\alpha\beta} = \sum_{\mathbf{k}}\langle c^\dagger_{\mathbf{k},\alpha}c_{\mathbf{k},\beta}\rangle$. Apart from a constant factor, the left-hand side is proportional to the spectral sum of the energy absorption rate for adiabatically switched pulses. We refer to above relation as the modulation sum rule.

We checked the modulation sum rule by integrating the energy absorption spectra presented earlier numerically and found it to be satisfied in all of the studied cases with an error of less than 1%, which was estimated to lie well within the error tolerance of numerical integrations.

V. EXPERIMENTAL OUTLOOK

Like numerous other theoretical predictions of many-body phenomena using polar molecules, the observation of the results presented in this paper may also be experimentally challenging. In this section, we discuss some of these challenges

and point out the experimental signatures that are expected to more robust.

The group at JILA has successfully realized a near-degenerate gas of KRb polar molecules with a density of $n \sim 4 \times 10^{11}$ cm^{-3}, a temperature of $T \simeq 1.4 T_F^{(0)}$ and a maximum dipole moment of $D \simeq 0.22$ Debye [6–10]. Loading the gas into a one-dimensional optical lattice with a wavelength of ~ 1 μm yields stacks of pancakes with $\sqrt{n} a_\perp \simeq 0.2$ and $r_d \simeq 0.04$, closely matching the parameters used to obtain the higher-temperature plots in Fig. 7.

In the experiments with KRb and generally all species with energetically favorable two-body chemical reactions, the molecules have a finite lifetime due to head-to-tail collisions. Populating higher subbands generally results in higher reactive collision rates, making experiments more challenging. From this perspective, it is favorable to prepare the system in the single subband regime. The results shown in Fig. 6 belong to such a regime and, in particular, observation of the the excitonic peak is expected to be feasible. However, presence of heating noise and broadening of excitonic peaks due to inelastic scatterings and finite pulse durations may mask the p-h continuum, which has less than 1% of the spectral weight. If only a single peak is resolved, it can be difficult to judge if the peak is associated to the exciton. Therefore, one may need to look for signatures of excitons in the multisubband regime.

Quéméner *et al.* have recently studied chemical reaction rates of reactive polar molecules in pancake geometries and have shown that the suppression of chemical reactions remains effective even if the first few excited subbands are populated [44]. Experiments with nonreactive polar molecules are another possibility for realizing multisubband systems with long lifetimes.

In the multisubband regime, a more robust experimental signature for excitonic effects can be found in the plots shown in Fig. 8. The appearance of two excitonic peaks (one mainly associated to $0 \to 2$ and the other to $1 \to 3$) and the disappearance of the first exciton upon relaxing the trap is expected to be detectable in both energy-resolved and band-resolved lattice modulation spectroscopy experiments. Most strikingly, the Fano interference effects reduce the spectral weight between the two excitons significantly [see Fig. 10(c2)] and allows the double-peak structure to be resolved even if the broadening of peaks is beyond their frequency separation. The plots in Figs. 8(b) and 10 suggest that observation of excitonic effects is not limited to strongly degenerate systems and is expected to be feasible for temperatures of the order of the Fermi temperature as well.

We note that extension of the band-resolved measurement technique to momentum-resolved measurements [61,62] can also be used to directly measure the exciton wave functions.

Although the band-resolved measurements yield valuable information about the nature of intersubband excitations, the energy-resolved measurements are generally expected to be less prone to broadening since they are not affected by quasiparticle relaxation processes.

Finally, we note that our choice of exponentially switched-on pulse shapes in this study was mainly for ease of calculations. Generally, the broadening of the peaks can be minimized by ramping up the amplitude of modulations as fast as possible, followed by a hold interval at the maximum amplitude.

VI. CONCLUSIONS

In this paper, we theoretically analyzed a quasi-two-dimensional system of fermionic polar molecules in a harmonic transverse confining potential. The electric dipole moments of the molecules were assumed to be aligned perpendicular to the confining plane using a strong dc electric field. We studied the renormalization of the energy bands in the Hartree-Fock approximation for various trap strengths, dipolar interaction strengths, and temperatures (Fig. 2). The renormalized subbands were found to be parity-conserving mixtures of the noninteracting subbands (Fig. 3). A phase diagram was obtained for the normal liquid phases of the system at zero temperature (Fig. 4) as a function of trap and interaction strengths.

We also studied the intersubband excitation spectrum of the system in the conserving time-dependent Hartree-Fock (TDHF) approximation for various system parameters and presented theoretical predictions for energy absorption rates in lattice modulation spectroscopy experiments. We found that the excitation spectrum consists of both intersubband p-h continua and antibound excitons (Figs. 6, 7, and 8). The excitons capture more than 99% of the spectral weight. Our results indicate that both types of excitations are present for interaction strengths and temperatures accessible in current experiments with polar molecules.

By evaluating the intersubband transition rates in lattice modulation spectroscopy experiments, we studied the nature of excitons and found that they are mixtures of p-h excitations arising from several subbands (Figs. 9 and 10). We also found a criterion for the validity of TDHF predictions for intersubband transition rates [Eq. (46)].

Finally, we briefly discussed the experimental outlook of this study and pointed out the most robust experimental signatures of excitonic effects based on the the presented results.

ACKNOWLEDGMENTS

The authors would like to thank Bertrand Halperin, Jun Ye, Deborah Jin, Sankar Das Sarma, Brian C. Sawyer, and David Pekker for insightful discussions. This work was supported by the Army Research Office with funding from the DARPA OLE program, Harvard-MIT CUA, NSF Grant No. DMR-07-05472, AFOSR Quantum Simulation MURI, AFOSR MURI on Ultracold Molecules, and the ARO-MURI on Atomtronics.

APPENDIX A: GENERATING FUNCTION FOR EFFECTIVE INTERSUBBAND DIPOLAR INTERACTIONS IN HARMONIC TRAPS

In this appendix, we derive a generating function for the effective intersubband dipolar interactions for harmonic traps and provide explicit formulas for the first few. We start the derivation by transforming the in-plane coordinates of

the electric dipole-dipole interaction [Eq. (5)] to momentum space:

$$\mathcal{V}_{\rm dip}(z,\mathbf{q}) = \int d^2\mathbf{x} e^{-i\mathbf{q}\cdot\mathbf{x}} V_{\rm dip}(z,\mathbf{x}) = \frac{8\pi D^2}{3}\delta(z) - 2\pi D^2|\mathbf{q}|e^{-|\mathbf{q}||z|}. \quad \text{(A1)}$$

The effective intersubband interaction is obtained by integrating out the z coordinate:

$$\mathcal{V}_{\alpha\beta;\gamma\lambda}(\mathbf{q}) = \int dz dz' \phi_\alpha(z)\phi_\beta(z)\phi_\gamma(z')\phi_\lambda(z')\mathcal{V}_{\rm dip}(z-z',\mathbf{q}) = \frac{8\pi D^2}{3}\int_{-\infty}^{\infty} dz \phi_\alpha(z)\phi_\beta(z)\phi_\gamma(z')\phi_\lambda(z') - 4\pi D^2|\mathbf{q}|\int_0^\infty d\xi \int_{-\infty}^{\infty} d\eta [\phi_\alpha(\eta+\xi)\phi_\beta(\eta+\xi) \times \phi_\gamma(\eta-\xi)\phi_\lambda(\eta-\xi) + \phi_\alpha(\eta-\xi)\phi_\beta(\eta-\xi) \times \phi_\gamma(\eta+\xi)\phi_\lambda(\eta+\xi)]e^{-2|\mathbf{q}|\xi}, \quad \text{(A2)}$$

where the transverse wave functions, $\phi_\alpha(z)$, etc., are the well-known harmonic oscillator wave functions [Eq. (6)]. We have changed variables to $\eta = (z+z')/2$ and $\xi = (z-z')/2$ in order to take care of the absolute value appearing in Eq. (A1) conveniently.

A generating function for $\mathcal{V}_{\alpha\beta;\gamma\lambda}(\mathbf{q})$ can be found by expressing the Hermite functions appearing in Eq. (6) in terms of their generating function:

$$e^{2xt-t^2} = \sum_{n=0}^{\infty}\frac{H_n(x)t^n}{n!}. \quad \text{(A3)}$$

Plugging Eq. (6) into Eq. (A2) and using Eq. (A3), we get the following generating function for $\mathcal{V}_{\alpha\beta;\gamma\lambda}(\mathbf{q})$:

$$\begin{aligned}\Gamma(w_1,w_2,w_3,w_4;\mathbf{q}) = {}& \frac{8D^2}{3a_\perp}\int_{-\infty}^{\infty} d\tilde{z} e^{2\tilde{z}w_1-w_1^2}e^{2\tilde{z}w_2-w_2^2}e^{2\tilde{z}w_3-w_3^2}e^{2\tilde{z}w_4-w_4^2}e^{-4\tilde{z}^2/2} - 4D^2|\mathbf{q}|\int_0^\infty d\xi\int_{-\infty}^{\infty} d\eta \\ & \times\left[e^{2(\eta+\xi)w_1-w_1^2}e^{2(\eta+\xi)w_2-w_2^2}e^{2(\eta-\xi)w_3-w_3^2}e^{2(\eta-\xi)w_4-w_4^2}e^{-(\eta+\xi)^2}e^{-(\eta-\xi)^2}\right. \\ & \left.+ e^{2(\eta-\xi)w_1-w_1^2}e^{2(\eta-\xi)w_2-w_2^2}e^{2(\eta+\xi)w_3-w_3^2}e^{2(\eta+\xi)w_4-w_4^2}e^{-(\eta+\xi)^2}e^{-(\eta-\xi)^2}\right]e^{-2|\mathbf{q}|\xi} \\ = {}& \frac{4\sqrt{2\pi}D^2}{3a_\perp}e^{-w_1^2-w_2^2-w_3^2-w_4^2+\frac{1}{2}(w_1+w_2+w_3+w_4)^2} - \pi D^2|\mathbf{q}|e^{|\mathbf{q}|^2a_\perp^2/2+2w_1w_2+2w_3w_4+|\mathbf{q}|a_\perp(w_1+w_2-w_3-w_4)} \\ & \times\mathrm{erfc}\left(\frac{|\mathbf{q}|a_\perp+w_1+w_2-w_3-w_4}{\sqrt{2}}\right) - \pi D^2|\mathbf{q}|e^{|\mathbf{q}|^2a_\perp^2/2+2w_3w_4+2w_1w_2+|\mathbf{q}|a_\perp(w_3+w_4-w_1-w_2)} \\ & \times\mathrm{erfc}\left(\frac{|\mathbf{q}|a_\perp+w_3+w_4-w_1-w_2}{\sqrt{2}}\right), \end{aligned} \quad \text{(A4)}$$

and $\mathcal{V}_{\alpha\beta;\gamma\lambda}(\mathbf{q})$ is given by

$$\mathcal{V}_{\alpha\beta;\gamma\lambda}(\mathbf{q}) = \left.\frac{\partial_{w_1}^\alpha\partial_{w_2}^\beta\partial_{w_3}^\gamma\partial_{w_4}^\lambda\Gamma(w_1,w_2,w_3,w_4;\mathbf{q})}{\sqrt{\alpha!\beta!\gamma!\lambda!2^\alpha 2^\beta 2^\gamma 2^\lambda}}\right|_{w_i=0}. \quad \text{(A5)}$$

Using Eq. (A5), we provide explicit expressions for the interactions between the first two subbands and their long-wavelength limits for reference:

$$\begin{aligned}\mathcal{V}_{00;00}(\mathbf{q}) &= \frac{4\sqrt{2\pi}D^2}{3a_\perp} - 2\pi D^2|\mathbf{q}|e^{|\mathbf{q}|^2a_\perp^2/2} \times\mathrm{erfc}(|\mathbf{q}|a_\perp/\sqrt{2}) \\ &\simeq \frac{4\sqrt{2\pi}D^2}{3a_\perp} - 2\pi D^2|\mathbf{q}| + O(|\mathbf{q}|^2), \end{aligned} \quad \text{(A6)}$$

$$\begin{aligned}\mathcal{V}_{01;01}(\mathbf{q}) &= \frac{\sqrt{2\pi}D^2}{3a_\perp}(2-3|\mathbf{q}|^2a_\perp^2) + \pi D^2|\mathbf{q}|^3a_\perp^2e^{|\mathbf{q}|^2a_\perp^2/2} \times\mathrm{erfc}(|\mathbf{q}|a_\perp/\sqrt{2}) \\ &\simeq \frac{2\sqrt{2\pi}D^2}{3a_\perp} - \sqrt{2\pi}D^2|\mathbf{q}|^2a_\perp + O(|\mathbf{q}|^3), \end{aligned} \quad \text{(A7)}$$

$$\begin{aligned}\mathcal{V}_{00;11}(\mathbf{q}) &= \frac{\sqrt{2\pi}D^2}{3a_\perp}(2+3|\mathbf{q}|^2a_\perp^2) - \pi D^2|\mathbf{q}|(2+|\mathbf{q}|^2a_\perp^2) \times e^{|\mathbf{q}|^2a_\perp^2/2}\mathrm{erfc}(|\mathbf{q}|a_\perp/\sqrt{2}) \\ &\simeq \frac{2\sqrt{2\pi}D^2}{3a_\perp} - 2\pi D^2|\mathbf{q}| + O(|\mathbf{q}|^2), \end{aligned} \quad \text{(A8)}$$

$$\begin{aligned}\mathcal{V}_{11;11}(\mathbf{q}) &= \frac{\sqrt{2\pi}D^2}{2a_\perp}(1+|\mathbf{q}|^2a_\perp^2)(2+|\mathbf{q}|^2a_\perp^2) - \frac{\pi D^2}{2}|\mathbf{q}|(2+|\mathbf{q}|^2a_\perp^2)^2e^{|\mathbf{q}|^2a_\perp^2/2}\mathrm{erfc}(|\mathbf{q}|a_\perp/\sqrt{2}) \\ &\simeq \frac{\sqrt{2\pi}D^2}{a_\perp} - 2\pi D^2|\mathbf{q}| + O(|\mathbf{q}|^2). \end{aligned} \quad \text{(A9)}$$

Note that $\mathcal{V}_{01;01} = \mathcal{V}_{10;01} = \mathcal{V}_{10;10} = \mathcal{V}_{01;10}$, $\mathcal{V}_{00;11} = \mathcal{V}_{11;00}$ and $\mathcal{V}_{00;01} = \mathcal{V}_{00;10} = \mathcal{V}_{01;00} = \mathcal{V}_{10;00} = 0$.

APPENDIX B: NUMERICAL SOLUTION OF HARTREE-FOCK EQUATION

Our goal is to develop a numerical routine to find a self-consistent solution to Eq. (17) at any given temperature, dipolar

interaction strength, and transverse confinement strength. In its current form, Eq. (17) describes an infinite number of coupled nonlinear integral equations. However, we note that, at zero temperature, there is only a finite number of occupied subbands due to the sharp step-like behavior of Fermi occupation function. At finite temperatures, we also expect to find a finite number of subbands with a significant population. Thus, a cutoff can be imposed on the number of subbands in practice. In our implementation, we choose the cutoff such that the fractional density of the highest neglected subband is less than 10^{-3}. This ensures that the presence of higher subbands have a negligible effect (i.e., of the order of $10^{-3}D^2k_F^3$) on the energies of the lower subbands [see Eq. (17)]. The number of dimensions of the integral equations can also be reduced due to the isotropy of the intersubband interactions, which is inherited by the self-energy matrices and their related quantities. The self-consistent Hartree-Fock self-energy equation can be rewritten as

$$\Sigma^{\star}_{\mu\nu}(k) = \int \frac{k'dk'}{2\pi}[\mathcal{W}_{\mu\nu;\gamma\lambda}(0,0) - \mathcal{W}_{\mu\lambda;\gamma\nu}(k,k')]U(k')_{\lambda\rho} \times U(k')_{\gamma\rho}n^F[\xi_\rho(k')], \tag{B1}$$

where $\mathcal{W}_{\mu\lambda;\gamma\nu}(k,k')$ is the angle-averaged interaction, which is defined as

$$\mathcal{W}_{\mu\lambda;\gamma\nu}(k,k') = \int_0^{2\pi} \frac{d\phi}{2\pi}\mathcal{V}_{\mu\lambda;\gamma\nu}(\sqrt{q^2+k^2-2qk\cos\phi}). \tag{B2}$$

From a numerical perspective, it is favorable to deal with integrals with bounded integration domains. Although the momentum integral appearing in Eq. (B1) is unbounded, an upper bound can be imposed on it in a controlled way. Since the subbands have (approximately) a quadratic energy dispersion for large momenta, the Fermi occupation of states falls super-exponentially fast for large k' and the integral kernel of Eq. (B1) becomes negligible for large k'. In our implementation, we impose a large momentum cutoff K_{cut} such that $n^F[\xi_\rho(k')] < 10^{-6}$ for all $k' \geqslant K_{\text{cut}}$. Finally, we approximate the resulting bounded integrations using quadrature formulas:

$$\Sigma^{\star}(k_i)_{\mu\nu} = \sum_{j=1}^{N_p} \frac{w_j k'_j}{2\pi}[\mathcal{V}_{\mu\nu;\gamma\lambda}(0) - \mathcal{W}_{\mu\lambda;\gamma\nu}(k_i,k'_j)] \times U(k'_j)_{\lambda\rho}U(k'_j)_{\gamma\rho}n^F[\xi_\rho(k'_j)], \quad i = 1,\ldots,N_p, \tag{B3}$$

where k_i and w_i denote the quadrature nodes and weights respectively and N_p is the number of quadrature points. We used a 200-point Gauss-Lobatto quadrature in our implementation [63].

It is desirable from an experimental perspective to solve the Hartree-Fock equation for a given particle density n instead of the chemical potential μ. Therefore, the chemical potential must be found in a such a way that the self-energy equation [Eq. (B3)] and particle density equation

$$n = \sum_\rho \int \frac{d^2\mathbf{k}}{(2\pi)^2}n^F[\xi_\rho(\mathbf{k})] \simeq \sum_\rho \sum_{j=1}^{N_p} \frac{w_j k_j}{2\pi}n^F[\xi_\rho(k_j)] \tag{B4}$$

are satisfied simultaneously. We found it more efficient to solve the system of nonlinear equations [Eqs. (B3) and (B4)] using an interior reflective trust region method [64] instead of the usual solution by iterations. In all of the runs, the solution was unique and the convergence was rapid.

APPENDIX C: ENERGY ABSORPTION RATE FOR EXPONENTIALLY SWITCHED-ON AC MODULATION PULSE

In this appendix, we derive the formula given for the energy absorption rate for an exponentially switched-on ac modulation pulse in Sec. IV [Eq. (33)]. Our strategy is to evaluate the total absorbed energy for a given pulse shape ΔE. We define the energy absorption rate as $\Delta E/\Delta t$, where Δt is the effective time interval during which the external field interacts with the system. For the exponentially switched-on and -off pulse of Eq. (32), $\Delta t \sim 2\eta^{-1}$. We start with Eq. (28), which we integrate with respect to time to obtain ΔE:

$$\Delta E = i\xi^2 \int_{-\infty}^{\infty} dt f(t) \int_{-\infty}^{\infty} dt' f(t')\partial_t \mathcal{T}(t-t') = i\xi^2 \int \frac{d\omega}{2\pi}|f(\omega)|^2\omega\mathcal{T}(\omega). \tag{C1}$$

Here, $f(\omega)$ is the Fourier transform of Eq. (32). We write $|f(\omega)|^2$ as

$$|f(\omega)|^2 = f_+^2(\omega) + f_-^2(\omega) + 2f_+(\omega)f_-(\omega), \tag{C2}$$

where

$$f_\pm(\omega) = \frac{\eta}{\eta^2 + (\omega \mp \Omega)^2}. \tag{C3}$$

First, we focus on the contributions of $f_\pm^2(\omega)$ to ΔE. This function has two second-order poles at frequencies $\mp\Omega + i\eta$ and $\pm\Omega - i\eta$. Since $\mathcal{T}(t)$ is a causal function, $\mathcal{T}(\omega)$ is analytic in the upper complex plane and the integral in the second line of Eq. (C1) can be evaluated by closing the contour on the upper half plane. The resulting contribution is easily found to be

$$\Delta E_\pm \equiv -\xi^2\eta^2\left[\frac{\mathcal{T}(\pm\Omega+i\eta)}{(2i\eta)^2} + \frac{(\pm\Omega+i\eta)\mathcal{T}'(\pm\Omega+i\eta)}{(2i\eta)^2} - \frac{2(\pm\Omega+i\eta)\mathcal{T}(\pm\Omega+i\eta)}{(2i\eta)^3}\right], \tag{C4}$$

where $\mathcal{T}'(\omega) = (d/d\omega)\mathcal{T}(\omega)$.

The contribution of the cross-term, $2f_+(\omega)f_-(\omega)$, to ΔE can be evaluated in the same way:

$$\Delta E_c \equiv \frac{i\xi^2\eta}{8\Omega}[\mathcal{T}(\Omega+i\eta) - \mathcal{T}(-\Omega+i\eta)]. \tag{C5}$$

Using Eqs. (29), (30), (38), and (39), it is straightforward to establish the following identities:

$$\begin{aligned} \mathcal{T}(\omega) &= \mathcal{T}(-\omega), \\ \mathcal{T}(\omega^*) &= \mathcal{T}(\omega)^*, \\ \mathcal{T}'(\omega) &= -\mathcal{T}'(-\omega), \\ \mathcal{T}'(\omega^*) &= \mathcal{T}'(\omega)^*, \end{aligned} \tag{C6}$$

using which we get $\mathcal{T}(-\Omega+i\eta)=\mathcal{T}(\Omega+i\eta)^*$ and $\mathcal{T}'(-\Omega+i\eta)=-\mathcal{T}'(\Omega+i\eta)^*$. Using these identities, we get the following simple expression for $\dot{E}=\eta\Delta E/2\equiv\eta(\Delta E_+ + \Delta E_- + \Delta E_c)/2$:

$$\dot{E}=-\frac{\xi^2}{4}\Omega\mathrm{Im}[\mathcal{T}(\Omega+i\eta)]+\frac{\eta\xi^2}{4}\mathrm{Re}[(\Omega+i\eta)\mathcal{T}'(\Omega+i\eta)]. \tag{C7}$$

In the limit $\eta/\Omega\ll 1$, the second term is negligible and we get the desired result [Eq. (33)].

APPENDIX D: ESTIMATION OF RELAXATION RATE OF INTERSUBBAND *p-h* EXCITATIONS

In this appendix, we estimate the relaxation rate of intersubband p-h excitations created by the lattice modulation pulse. As mentioned in the final remarks of Sec. IV A, such relaxation processes are absent in the TDHF approximation. Therefore, predictions of TDHF approximation for the intersubband transition rates are only valid if the lifetime of excitations is longer than the pulse duration [see Eq. (46)].

For weak interactions, we expect the relaxation rate of both types of intersubband excitations, quasiparticle-like excitations, and excitons, to be of the same order. We only study the former case here. We are interested in relaxation processes that change the population of subbands and, therefore, we neglect the intrasubband scatterings.

Relaxation of a quasiparticle excitation can occur through several channels. The number of relaxation channels is higher for quasiparticles in higher subbands. As mentioned in Sec. II, the intersubband interaction matrix elements conserve the net parity of the interacting particles and this condition constrains the number of relaxation channels. A simple counting shows that the number of relaxation channels scales like $\sim N^3/4$, where N is the subband index of the decaying quasiparticle. Although the number of relaxation channels grows rapidly with N, one can still argue that the fastest relaxation processes of an excitation in any given subband are those that involve the first few subbands just below it. The reason is twofold: (1) the intersubband interaction between particles in well-separated subbands is small and (2) the lower subbands have larger Fermi momenta and, consequently, creating a quasiparticle excitation in them upon deexciting the original quasiparticle has a higher energy cost. Therefore, the quasiparticle relaxation rate of particles in the higher subbands are expected to be essentially of the same order as those in the lower subbands.

We study the relaxation of a quasiparticle excitation in the second excited subband as a concrete example. Based on the above argument, we expect this rate to be representative of the relaxation rate of quasiparticles in higher subbands as well. Figure 11 shows the three relaxation processes that that contribute to the decay. Since the interactions are assumed to be weak ($r_d\ll 1$), Born's approximation is applicable. We ignore the self-energy correction since such corrections are beyond Born's approximation. The initial and final wave functions of the system in all of the processes shown in Fig. 12 can be written as $|i\rangle=\tilde{c}^\dagger_{\mathbf{p}_0,\lambda}\tilde{c}_{\mathbf{p}_0,\alpha}|\Psi_0\rangle$ and $|f\rangle=\tilde{c}^\dagger_{\mathbf{p}_1,\gamma}\tilde{c}^\dagger_{\mathbf{p}'_1,\mu}\tilde{c}_{\mathbf{p}'_0,\nu}\tilde{c}_{\mathbf{p}_0,\alpha}|\Psi_0\rangle$, respectively, where $|\Psi_0\rangle$ is the Fermi

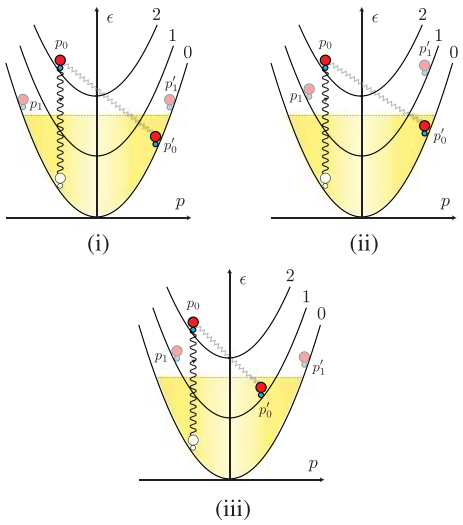

FIG. 11. (Color online) The three relaxation processes contributing to Γ_2^{rel}.

gaslike ground state of the system. The rate of this generic process can be obtained using Fermi's golden rule:

$$\begin{aligned}&\Gamma_{\gamma\lambda;\mu\nu}(\mathbf{p}_0,\mathbf{p}'_0,\mathbf{p}_1,\mathbf{p}'_1)\\&=\frac{8\pi^3}{A^3}|\tilde{\mathcal{V}}_{\gamma\lambda;\mu\nu}(\mathbf{p}_1-\mathbf{p}_0)-\tilde{\mathcal{V}}_{\mu\lambda;\gamma\nu}(\mathbf{p}'_1-\mathbf{p}_0)|^2\\&\times\delta(\mathbf{p}_0+\mathbf{p}'_0-\mathbf{p}_1-\mathbf{p}'_1)\times\delta(\tilde{\xi}_\lambda(\mathbf{p}_0)+\tilde{\xi}_\nu(\mathbf{p}'_0)-\tilde{\xi}_\gamma(\mathbf{p}_1)\\&-\tilde{\xi}_\mu(\mathbf{p}'_1))[1-n_\gamma(\mathbf{p}_1)][1-n_\mu(\mathbf{p}'_1)]n_\nu(\mathbf{p}'_0).\end{aligned} \tag{D1}$$

We work in units in which $\hbar=1$ in this appendix. Since the particles are identical, $\Gamma_{\gamma\lambda;\mu\nu}=\Gamma_{\mu\lambda;\gamma\nu}$ and over counting must be carefully avoided. The total contribution of this process can be found by summing over $\mathbf{p}'_0$, $\mathbf{p}_1$, and $\mathbf{p}'_1$. After lengthy but straightforward algebra, we obtain

$$\begin{aligned}\Gamma_{\gamma\lambda;\mu\nu}(\mathbf{p}_0)&\equiv A^3\int\frac{d^2\mathbf{p}'_0}{(2\pi)^2}\frac{d^2\mathbf{p}_1}{(2\pi)^2}\frac{d^2\mathbf{p}'_1}{(2\pi)^2}\gamma_{\gamma\lambda;\mu\nu}(\mathbf{p}_0,\mathbf{p}'_0,\mathbf{p}_1,\mathbf{p}'_1)\\&=\frac{m}{8\pi^3}\int_0^\infty Q\,dQ\int_0^{2\pi}d\phi\int_0^{2\pi}d\psi\\&\times\left|\mathcal{V}_{\gamma\lambda;\mu\nu}\left(\frac{1}{2}[\mathbf{Q}+\mathbf{q}_0-\mathbf{p}_0]\right)\right.\\&\left.-\mathcal{V}_{\mu\lambda;\gamma\nu}\left(\frac{1}{2}[\mathbf{Q}-\mathbf{q}_0-\mathbf{p}_0]\right)\right|^2\\&\times n_\nu(\mathbf{Q})\left[1-n_\gamma\left(\frac{1}{2}[\mathbf{Q}+\mathbf{q}_0+\mathbf{p}_0]\right)\right]\\&\times\left[1-n_\mu\left(\frac{1}{2}[\mathbf{Q}-\mathbf{q}_0+\mathbf{p}_0]\right)\right],\end{aligned} \tag{D2}$$

where $\mathbf{Q}=Q(\cos\phi\,\hat{\boldsymbol{x}}+\sin\phi\,\hat{\boldsymbol{y}})$, $\mathbf{q}_0=q_0(\cos\psi\,\hat{\boldsymbol{x}}+\sin\psi\,\hat{\boldsymbol{y}})$, and $q_0=[(\lambda+\nu-\gamma-\mu)2m\hbar\omega_{\mathrm{trap}}+|\mathbf{Q}-\mathbf{p}_0|^2]^{1/2}$. The total relaxation rate is obtained by summing over all channels:

$$\Gamma_2^{\mathrm{rel}}(\mathbf{p}_0)=\Gamma_{02;00}(\mathbf{p}_0)+\Gamma_{12;10}(\mathbf{p}_0)+\Gamma_{02;11}(\mathbf{p}_0). \tag{D3}$$

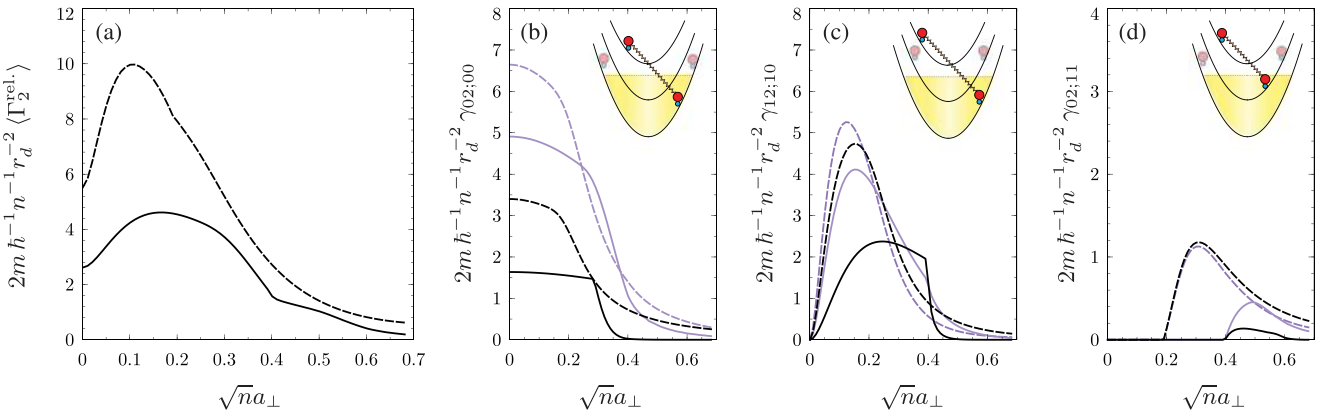

FIG. 12. (Color online) (a) Total momentum-averaged relaxation rate of a quasiparticle in the second-excited subband, $\langle\Gamma_2^{\rm rel}\rangle$ as function of transverse confinement width $a_\perp$. The solid and dashed lines correspond to $T=0$ and $T=10T^*$, respectively. Panels (b), (c), and (d) show the momentum-resolved contribution of different relaxation processes. The black and (light) blue plots correspond to $|\mathbf{p}_0|=0$ and $|\mathbf{p}_0|=p_{F,0}$, respectively, where $p_{F,0}\equiv\hbar\sqrt{4\pi n}$ is the Fermi momentum of the zeroth subband at zero temperature. The inset figures are graphical representations of the processes.

We define the momentum-averaged relaxation rate as

$$\left\langle\Gamma_2^{\rm rel}\right\rangle\equiv\frac{\int\frac{d^2\mathbf{p}}{(2\pi)^2}[n_0(\mathbf{p})-n_2(\mathbf{p})]\Gamma_2^{\rm rel}(\mathbf{p})}{\int\frac{d^2\mathbf{p}}{(2\pi)^2}[n_0(\mathbf{p})-n_2(\mathbf{p})]},\tag{D4}$$

where the averaging is weighted according to the momentum distribution of the p-h excitations generated by the lattice modulation pulse. For weak interactions, the number of excitations at momentum $\mathbf{p}$ is proportional to the equilibrium occupation of the states; that is, $\propto n_0(\mathbf{p})[1-n_2(\mathbf{p})]-n_2(\mathbf{p})[1-n_0(\mathbf{p})]=n_0(\mathbf{p})-n_2(\mathbf{p})$.

We evaluate the triple integral in Eq. (D2) numerically using an adaptive Monte Carlo integration algorithm. Figure 12(a) shows $\langle\Gamma_2^{\rm rel}\rangle$ as a function of transverse confinement width $a_\perp$ for $T=0$ and $T=10T^*$. Figures 12(b)–12(d) show the momentum-resolved rate of each of the relaxation processes as a function of $a_\perp$ for $|\mathbf{p}_0|=0$ and $|\mathbf{p}_0|=p_{F,0}$, where $p_{F,0}\equiv\hbar\sqrt{4\pi n}$ is the Fermi momentum of the zeroth subband at zero temperature.

We find that the major contributions result from the first two processes, the former being dominant for stronger traps. Also, increasing the temperature and quasiparticle momenta naturally results in higher relaxation rates. According to Fig. 12(a), the highest relaxation rate is $\langle\Gamma_2^{\rm rel}\rangle_{\rm max}\approx 5r_d^2[\hbar n/(2m)]$ and $10r_d^2[\hbar n/(2m)]$ for $T=0$ and $T=10T^*$ respectively. Using these estimates and Eq. (46), and choosing $\eta\gtrsim 5r_d^2[\hbar n/(2m)]$, guarantees the predictions of TDHF approximation for intersubband transition rates to be reliable for temperatures up to $T=10T^*$. For $r_d=0.05$, we get $\eta\gtrsim 0.01[\hbar n/(2m)]$.

APPENDIX E: NUMERICAL EVALUATION OF $\tilde{h}_{\alpha\beta}(\omega)$

In this appendix, we discuss the numerical method used to solve Eq. (41). Our approach is similar to similar to that described in Appendix B (i.e., we approximate the integral equations using integral quadratures). However, given that the integral equation to be solved is linear, the resulting system of equations is also linear.

As a first step, we note that the dimension of the integral equations can be reduced due to the isotropy of the intersubband interactions, and Eq. (41) reduces to

$$\tilde{h}_{\alpha\beta}(k_1;\omega)=\tilde{\mathbf{T}}_{\alpha\beta}(k_1)-\int\frac{k'dk'}{2\pi}\tilde{\mathcal{V}}^{(\rm d+e)}_{\alpha\beta;\mu\nu}(k_1,k')\times\tilde{\Pi}^{(0)}_{\mu\nu}(k';\omega)\tilde{h}_{\mu\nu}(k';\omega),\tag{E1}$$

where

$$\begin{aligned}\tilde{\mathcal{V}}^{(\rm d+e)}_{\alpha\beta;\mu\nu}(k,k')&=\int_0^{2\pi}\frac{d\phi_{\mathbf{k}'}}{2\pi}\tilde{\mathcal{U}}^{(\rm d+e)}_{\alpha\beta;\mu\nu}(\mathbf{k},\mathbf{k}')\\&=\int_0^{2\pi}\frac{d\phi_{\mathbf{k}'}}{2\pi}[\tilde{\mathcal{V}}_{\nu\beta;\alpha\mu}(k,k',\sqrt{k^2+k'^2-2kk'\cos\phi'_{\mathbf{k}}})\\&\quad-\tilde{\mathcal{V}}_{\alpha\beta;\nu\mu}(k,k',0)].\end{aligned}\tag{E2}$$

First, we study the subtler case of adiabatic switching ($\eta\to 0$) for which $\omega=\Omega+i\eta\to\Omega+i0^+$. In this limit, it is useful to separate the regular and singular parts of $\tilde{\Pi}^{(0)}_{\alpha\beta}(k',\omega)$:

$$\tilde{\Pi}^{(0)}_{\alpha\beta}(k',\omega)=\mathrm{P}\frac{n_\beta(k)-n_\alpha(k)}{\omega+\tilde{\xi}_\beta(k)-\tilde{\xi}_\alpha(k)}-i\pi[n_\beta(k)-n_\alpha(k)]\times\delta(\Omega+\tilde{\xi}_\beta(k)-\tilde{\xi}_\alpha(k)).\tag{E3}$$

where P denotes the Cauchy's principal value integration. The δ function may also be written as

$$\delta(\Omega+\tilde{\xi}_\beta(k)-\tilde{\xi}_\alpha(k))=\sum_j\frac{\delta(k-q_j)}{|\tilde{\xi}'_\alpha(q_j)-\tilde{\xi}'_\beta(q_j)|},\tag{E4}$$

where $\{q_j\}$ is the set of solutions of $\Omega+\tilde{\xi}_\beta(q)-\tilde{\xi}_\alpha(q)=0$. Inserting Eqs. (E3) and (E4) into Eq. (E1) and approximating the principal value integrals using quadratures, we get

$$\tilde{h}_{\alpha\beta}\big(k_i^{\alpha\beta};\omega\big)=\delta_{\alpha\gamma}\delta_{\beta\lambda}\tilde{\mathbf{T}}_{\alpha\beta}\big(k_i^{\alpha\beta}\big)-\sum_{\mu\nu}\sum_{j=1}^{N_p^{\mu\nu}}\left[\frac{w_j^{\mu\nu}k_j^{\mu\nu}}{2\pi}\tilde{\mathcal{V}}^{(\rm d+e)}_{\alpha\beta;\mu\nu}\times\big(k_i^{\alpha\beta},k_j^{\mu\nu}\big)\frac{n_\nu\big(k_j^{\mu\nu}\big)-n_\mu\big(k_j^{\mu\nu}\big)}{\omega+\tilde{\xi}_\nu\big(k_j^{\mu\nu}\big)-\tilde{\xi}_\mu\big(k_j^{\mu\nu}\big)}\right.$$

$$\times \tilde{h}_{\mu\nu}\left(k_j^{\mu\nu};\omega\right)\Bigg] + \frac{i}{2}\sum_{\mu\nu}\sum_{q_j^{\mu\nu}} \times \left[q_j^{\mu\nu}\,\frac{n_\nu\left(q_j^{\mu\nu}\right)-n_\mu\left(q_j^{\mu\nu}\right)}{\left|\tilde{\xi}'_\mu\left(q_j^{\mu\nu}\right)-\tilde{\xi}'_\nu\left(q_j^{\mu\nu}\right)\right|}\tilde{\mathcal{W}}^{(\mathrm{d+e})}_{\alpha\beta;\mu\nu}\left(k_i^{\alpha\beta},q_j^{\mu\nu}\right) \times \tilde{h}_{\mu\nu}\left(q_j^{\mu\nu};\omega\right)\right], \tag{E5}$$

where $\{k_i^{\alpha\beta}\}$ and $\{w_i^{\alpha\beta}\}$ are quadrature nodes and weights for the principal value integrals involving $\tilde{h}_{\alpha\beta;\ldots}$, $N_p^{\alpha\beta}$ is the number of corresponding nodes, and $\{q_j^{\mu\nu}\}$ is the set of solutions of $\Omega+\tilde{\xi}_\nu(q)-\tilde{\xi}_\mu(q)=0$.

In the case of finite switching rate ($\eta>0$), $\omega=\Omega+i\eta$ and $\tilde{\Pi}^{(0)}_{\alpha\beta}(k,\omega)$ is regular on the real axis. Therefore, the last term in Eq. (E5) arising from the poles on the real axis will be absent.

In our implementation, we imposed a large momentum cutoff on the integrals based on the same criteria as described in Appendix B. Quadratures for principal value integrations were generated using a combination of 16th-order Gauss-Lobatto quadrature in the proximity of the singular points and the Simpson rule elsewhere [63]. The resulting complex linear system of equations was solved for $h_{\alpha\beta}(k_i^{\alpha\beta},\omega)$ and, consequently, the function $\mathcal{T}(\omega)$ was evaluated using the discretized version of Eq. (42):

$$\mathcal{T}(\omega) = -\eta^2\omega\sum_{\alpha\beta}\Bigg[\sum_{k_i^{\alpha\beta}}\frac{w_i^{\alpha\beta}k_i^{\alpha\beta}}{2\pi}\tilde{\mathbf{T}}_{\alpha\beta}\left(k_i^{\alpha\beta}\right) \times \frac{n_\beta\left(k_i^{\alpha\beta}\right)-n_\alpha\left(k_i^{\alpha\beta}\right)}{\omega+\tilde{\xi}_\beta\left(k_i^{\alpha\beta}\right)-\tilde{\xi}_\alpha\left(k_i^{\alpha\beta}\right)}\tilde{h}_{\alpha\beta;\gamma\lambda}\left(k_i^{\alpha\beta};\omega\right) - \frac{i}{2}\sum_{q_i^{\alpha\beta}} q_i^{\alpha\beta}\mathbf{T}_{\alpha\beta}\left(q_i^{\alpha\beta}\right)\frac{n_\beta\left(q_i^{\alpha\beta}\right)-n_\alpha\left(q_i^{\alpha\beta}\right)}{\left|\tilde{\xi}'_\alpha\left(q_i^{\alpha\beta}\right)-\tilde{\xi}'_\beta\left(q_i^{\alpha\beta}\right)\right|} \times \tilde{h}_{\alpha\beta}\left(q_i^{\alpha\beta};\omega\right)\Bigg]. \tag{E6}$$

Again, the last term is absent for finite switching rates.

Once $\tilde{h}_{\alpha\beta}(\omega)$ and $\mathcal{T}(\omega)$ are found, the energy absorption spectrum, the spectral weight of excitons, and the intersubband transition rates can be readily evaluated using Eq. (33), (43), and (44), respectively. For finite pulse switching rates, the excitons will be broadened and Eq. (33) yields the full spectrum, including the broadened excitons, and Eq. (43) is no longer needed.

[1] M. Lewenstein, A. Sanpera, V. Ahufinger, B. Damski, A. Sen, and U. Sen, Adv. Phys. **56**, 243 (2007).

[2] I. Bloch, J. Dalibard, and W. Zwerger, Rev. Mod. Phys. **80**, 885 (2008).

[3] W. Ketterle and M. W. Zwierlein, *Ultracold Fermi Gases, Proceedings of the International School of Physics "Enrico Fermi," Course CLXIV, Varenna, 20–30 June, 2006*, edited by M. Inguscio, W. Ketterle, and C. Salomon (IOS Press, Amsterdam, 2008).

[4] F. Lang, K. Winkler, C. Strauss, R. Grimm, and J. Hecker Denschlag, Phys. Rev. Lett. **101**, 133005 (2008).

[5] J. Deiglmayr, A. Grochola, M. Repp, K. Mortlbauer, C. Gluck, J. Lange, O. Dulieu, R. Wester, and M. Weidemuller, Phys. Rev. Lett. **101**, 133004 (2008).

[6] S. Ospelkaus, A. Peer, K.-K. Ni, J. J. Zirbel, B. Neyen- huis, S. Kotochigova, P. S. Julienne, J. Ye, and D. S. Jin, Nat. Phys. **4**, 622 (2008).

[7] K.-K. Ni, S. Ospelkaus, M. H. G. de Miranda, A. Peer, B. Neyenhuis, J. J. Zirbel, S. Kotochigova, P. S. Julienne, D. S. Jin, and J. Ye, Science **322**, 231 (2008).

[8] K.-K. Ni, S. Ospelkaus, D. J. Nesbitt, J. Ye, and D. S. Jin, Phys. Chem. Chem. Phys. **11**, 9626 (2009).

[9] S. Ospelkaus, K.-K. Ni, D. Wang, M. H. G. de Miranda, B. Neyenhuis, G. Quéméner, P. S. Julienne, J. L. Bohn, D. S. Jin, and J. Ye, Science **327**, 853 (2010).

[10] K.-K. Ni, S. Ospelkaus, D. Wang, G. Quéméner, B. Neyenhuis, M. H. G. de Miranda, J. L. Bohn, J. Ye, and D. S. Jin, Nature (London) **464**, 1324 (2010).

[11] H. P. Büchler, E. Demler, M. Lukin, A. Micheli, N. Prokof'ev, G. Pupillo, and P. Zoller, Phys. Rev. Lett. **98**, 060404 (2007).

[12] A. Micheli, G. K. Brennen, and P. Zoller, Nat. Phys. **2**, 341 (2006).

[13] M. Ortner, A. Micheli, G. Pupillo, and P. Zoller, New J. Phys. **11**, 055045 (2009).

[14] L. Santos, G. V. Shlyapnikov, and M. Lewenstein, Phys. Rev. Lett. **90**, 250403 (2003).

[15] S. Ronen, D. C. E. Bortolotti, and J. L. Bohn, Phys. Rev. Lett. **98**, 030406 (2007).

[16] D.-W. Wang and E. Demler, e-print arXiv:0812.1838.

[17] P. Sengupta, L. P. Pryadko, F. Alet, M. Troyer, and G. Schmid, Phys. Rev. Lett. **94**, 207202 (2005).

[18] M. Boninsegni and N. Prokof'ev, Phys. Rev. Lett. **95**, 237204 (2005).

[19] B. Capogrosso-Sansone, C. Trefzger, M. Lewenstein, P. Zoller, and G. Pupillo, Phys. Rev. Lett. **104**, 125301 (2010).

[20] L. Pollet, J. D. Picon, H. P. Büchler, and M. Troyer, Phys. Rev. Lett. **104**, 125302 (2010).

[21] F. J. Burnell, M. M. Parish, N. R. Cooper, and S. L. Sondhi, Phys. Rev. B **80**, 174519 (2009).

[22] G. M. Bruun and E. Taylor, Phys. Rev. Lett. **101**, 245301 (2008).

[23] S. Tewari, V. W. Scarola, T. Senthil, and S. Das Sarma, Phys. Rev. Lett. **97**, 200401 (2006).

[24] D.-W. Wang, Phys. Rev. Lett. **98**, 060403 (2007).

[25] D.-W. Wang, M. D. Lukin, and E. Demler, Phys. Rev. Lett. **97**, 180413 (2006).

[26] A. C. Potter, E. Berg, D.-W. Wang, B. I. Halperin, and E. Demler, Phys. Rev. Lett. **105**, 220406 (2010).

[27] M. A. Baranov, A. Micheli, S. Ronen, and P. Zoller, Phys. Rev. A **83**, 043602 (2011).

[28] Roman M. Lutchyn, Enrico Rossi, and S. Das Sarma, e-print arXiv:0911.1378v1.

[29] M. Iskin and C. A. R. Sá de Melo, Phys. Rev. Lett. **99**, 110402 (2007).
[30] C.-H. Lin, Y.-T. Hsu, H. Lee, and D.-W. Wang, Phys. Rev. A **81**, 031601 (2010).
[31] T. Sogo, L. He, T. Miyakawa, S. Yi, H. Lu, and H. Pu, New J. Phys. **11**, 055017 (2009).
[32] T. Miyakawa, T. Sogo, and H. Pu, Phys. Rev. A **77**, 061603 (2008).
[33] C.-K. Chan, C.-J. Wu, W.-C. Lee, and S. Das Sarma, Phys. Rev. **81**, 023602 (2010).
[34] S. Ronen and J. L. Bohn, Phys. Rev. A **81**, 033601 (2010).
[35] M. A. Baranov, K. Osterloh, and M. Lewenstein, Phys. Rev. Lett. **94**, 070404 (2005).
[36] M. A. Baranov, H. Fehrmann, and M. Lewenstein, Phys. Rev. Lett. **100**, 200402 (2008).
[37] Y. Yamaguchi, T. Sogo, T. Ito, and T. Miyakawa, Phys. Rev. A **82**, 013643 (2010).
[38] K. Sun, C. Wu, and S. Das Sarma, Phys. Rev. B **82**, 075105 (2010).
[39] B. M. Fregoso, K. Sun, E. Fradkin, and B. L. Lev, New J. Phys. **11**, 103003 (2009).
[40] N. R. Cooper and G. V. Shlyapnikov, Phys. Rev. Lett. **103**, 155302 (2009).
[41] K. Sun, E. Zhao, and W. V. Liu, Phys. Rev. Lett. **104**, 165303 (2010).
[42] P. S. Zuchowski and J. M. Hutson, Phys. Rev. A **81**, 060703 (2010).
[43] G. Quéméner and J. L. Bohn, Phys. Rev. A **81**, 022702 (2010).
[44] G. Quéméner and J. L. Bohn, Phys. Rev. A **83**, 012705 (2011).
[45] T. Stöferle, H. Moritz, C. Schori, M. Köhl, and T. Esslinger, Phys. Rev. Lett. **92**, 130403 (2004).
[46] A. Iucci, M. A. Cazalilla, A. F. Ho, and T. Giamarchi, Phys. Rev. **A 73**, 041608 (2006).
[47] C. Kollath, A. Iucci, T. Giamarchi, W. Hofstetter, and U. Schollwöck, Phys. Rev. Lett. **97**, 050402 (2006).
[48] R. Sensarma, D. Pekker, M. D. Lukin, and E. Demler, Phys. Rev. Lett. **103**, 035303 (2009).
[49] A. Tokuno, E. Demler, and T. Giamarchi, e-print arXiv:1106.1333.
[50] G. Baym and L. P. Kadanoff, Phys. Rev. **124**, 287 (1961).
[51] G. B. Arfken, H. J. Weber, and F. Harris, *Mathematical Methods for Physicists*, 5th ed. (Academic Press, San diego, 2000).
[52] B. M. Fregoso and E. Fradkin, Phys. Rev. B **81**, 214443 (2010).
[53] A. L. Fetter and J. D. Walecka, *Quantum Theory of Many-Particle Systems*, 5th ed. (Dover Publications, Mineola, 2003).
[54] A. R. Goni, U. Haboeck, C. Thomsen, K. Eberl, F. A. Reboredo, C. R. Proetto, and F. Guinea, Phys. Rev. B **65**, 121313 (2002).
[55] J. P. Kestner and S. Das Sarma, Phys. Rev. A **82**, 033608 (2010).
[56] P. Nozieres and D. Pines, *Theory of Quantum Liquids* (Westview Press, Cambridge, MA, 1999).
[57] K. Takayanagi and E. Lipparini, Phys. Rev. B **52**, 1738 (1995).
[58] G. D. Mahan, *Many-Particle Physics*, 3rd ed. (Kluwer Academic/Plenum, New York, 1981).
[59] U. Fano, Phys. Rev. **124**, 1866 (1961).
[60] D. E. Nikonov, A. Imamoğlu, and M. O. Scully, Phys. Rev. B **59**, 12212 (1999).
[61] K. Winkler, G. Thalhammer, F. Lang, R. Grimm, J. Hecker Denschlag, A. J. Daley, A. Kantian, H. P. Büchler, and P. Zoller, Nature (London) **441**, 853 (2006).
[62] P. T. Ernst, S. Götze, J. S. Krauser, K. Pyka, D. Lühmann, D. Pfannkuche, and K. Sengstock, Nat. Phys. **6**, 74 (2010).
[63] M. Abramowitz and I. A. Stegun, *Handbook of Mathematical Functions (with Formulas, Graphs, and Mathematical Tables)* (Dover Publications, New York, 1965).
[64] T. F. Coleman and Y. Li, SIAM J. Opt. **6**, 418 (1996).